nature portfolio

https://doi.org/10.1038/s41586-023-06278-z

Supplementary information

All-perovskite tandem solar cells with 3D/3D bilayer perovskite heterojunction

In the format provided by the authors and unedited

Supplementary Information for:

All-perovskite tandem solar cells with 3D/3D bilayer perovskite heterojunction

Renxing Lin[1 †], Yurui Wang[1 †], Qianwen Lu[1 †], Beibei Tang[2], Jiayi Li[1], Han Gao[1], Yuan Gao[1], Hongjiang Li[1], Changzeng Ding[3], Jin Wen[1], Pu Wu[1], Chenshuaiyu Liu[1], Siyang Zhao[1], Ke Xiao[1], Zhou Liu[1], Changqi Ma[3], Yu Deng[1], Ludong Li[1], Fengjia Fan[2] and Hairen Tan[1*]

[1]*National Laboratory of Solid State Microstructures, College of Engineering and Applied Sciences, Frontiers Science Center for Critical Earth Material Cycling, Nanjing University, Nanjing 210023, China.*

[2]*School of Physical Sciences, University of Science and technology of China, Hefei 230026, China.*

[3]*i-Lab & Printable Electronics Research Center, Suzhou Institute of Nano-Tech and Nano-Bionics, Chinese Academy of Sciences (CAS), Suzhou 215123, China.*

† These authors contributed equally to this work.

E-mail: hairentan@nju.edu.cn

Contents

Supplementary Figs. 1-2

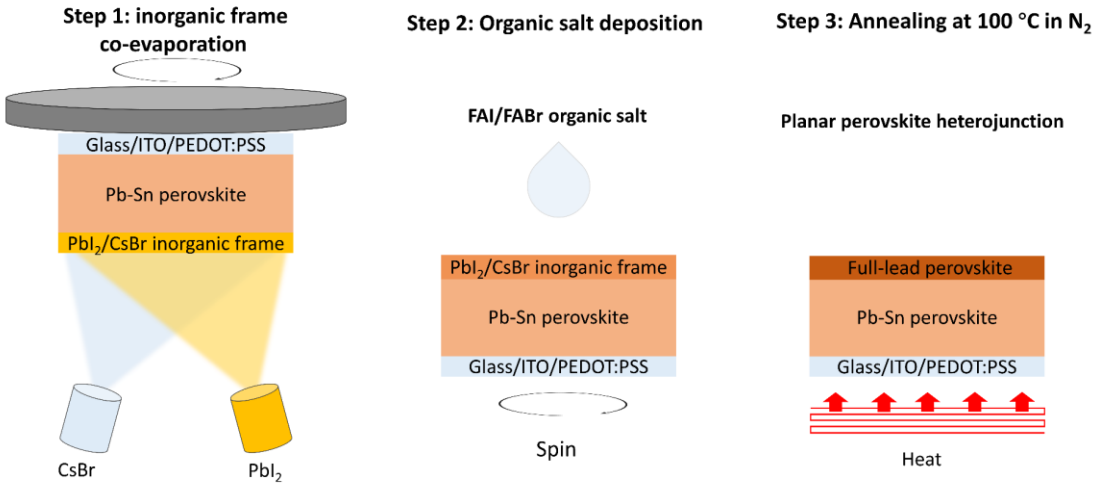

Supplementary Figure 1 | The preparation process of 3D/3D bilayer perovskite heterojunction mixed Pb-Sn perovskite solar cell. Two-step method for the deposition of FL-WBG perovskite on top of the Pb-Sn perovskite layer: first, thermal evaporation was used to deposit a mixed PbI_2 and CsBr layer on top of the Pb-Sn perovskite film; the inorganic framework was then converted to FL-WBG perovskites by spin-coating an organic-halide atop. As opposed to the full solution processing of perovskites, this evaporation/solution based hybrid method avoids dissolving the underlying perovskite layer by the high-polar solvents (such as dimethylformamide, DMF).

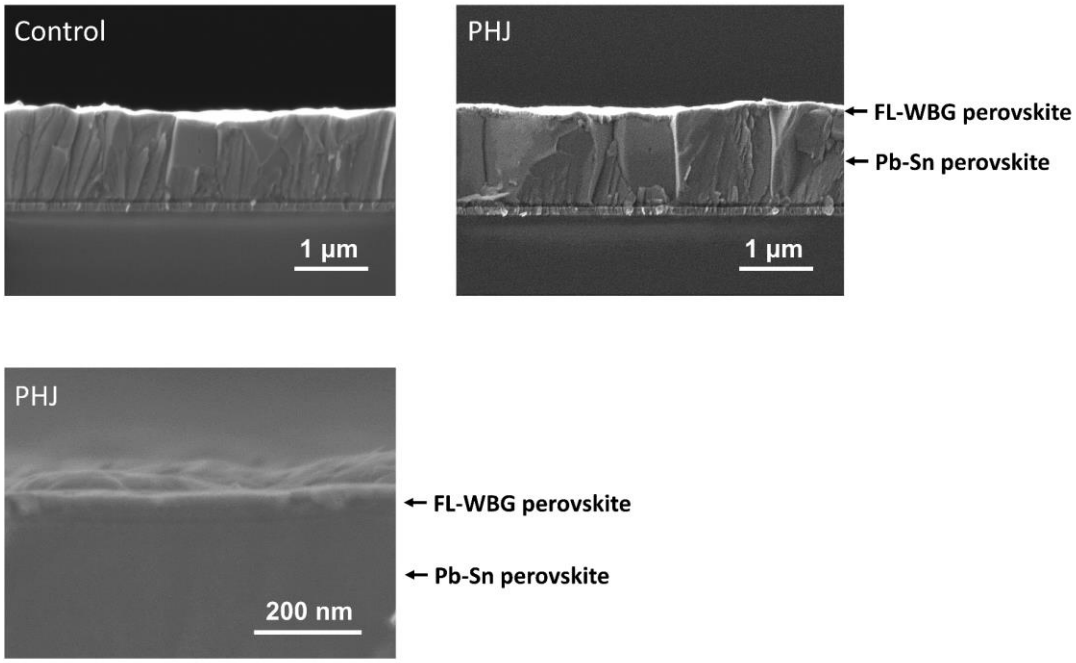

Supplementary Figure 2 | Cross-sectional SEM image of control and PHJ mixed Pb-Sn perovskite films. The thickness of the Pb-Sn perovskite absorber layer is about 1,200 nm (precursor concentration 2.4 M) and FL-WBG layer is about 50 nm.

Supplementary Note 1

To achieve a better effect of improving the performance of the Pb-Sn PSC with bilayer PHJ, we have optimized the FL-WBG. We prepared 3D/3D bilayer perovskite heterojunction structures on the surface of Pb-Sn perovskite by an evaporation-solution two-step method. We achieved suitable energy levels and dense coverage of the FL-WBG by adjusting the organic salt ratio and the content of Cs ions in the inorganic framework. We observed that the performance of heterojunction with FL-WBG prepared from organic salts of all-FAI and all-FABr was worse than control. Adjusting the ratio of FAI and FABr in the organic salt, the performance of the device is significantly improved (FABr/FAI=1/1 for the best device performance). (**Supplementary Figs 3, 4** and **Supplementary Table 1**). We observed enlargement of grain sizes and pinhole of the film surface for all-FAI and impurity for all-FABr (**Supplementary Fig 5a, c**). For film where FABr/FAI= 1/1, we observed the denser grain arrangement with a uniform surface, as observed from SEM (**Supplementary Fig 5b**). We further explored the effect of the ratio of PbI_2/CsBr in the inorganic layer on the device performance. We observed that with the increase of Cs, the V_{oc} of the device first increased and then decreased. When PbI_2/CsBr=2.5/1, the performance of the device is the best (**Supplementary Fig 6**). SEM images show that the grains of FL-WBG with a large amount of Cs are not clear and have poor crystallinity (yellow phase) and the grains of FL-WBG with a small amount of Cs are large and have pinholes, which cannot achieve complete coverage of the surface (**Supplementary Fig 7**). Finally, we optimize the thickness of the FL-WBG. The optimal concentrations of PbI_2/CsBr inorganic layer thickness was 30 nm (the thickness of FL-WBG ~50 nm) (**Supplementary Fig 8-9** and **Supplementary Table 2**).

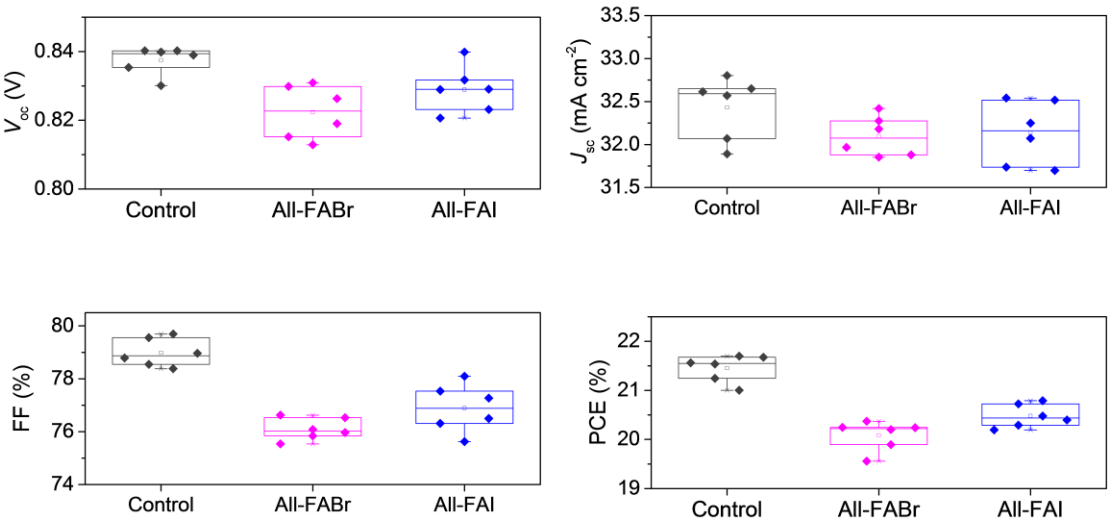

Supplementary Figure 3 | Performance of control and PHJ. The FL-WBG perovskite films with all-FABr and all-FAI in the organic salt.

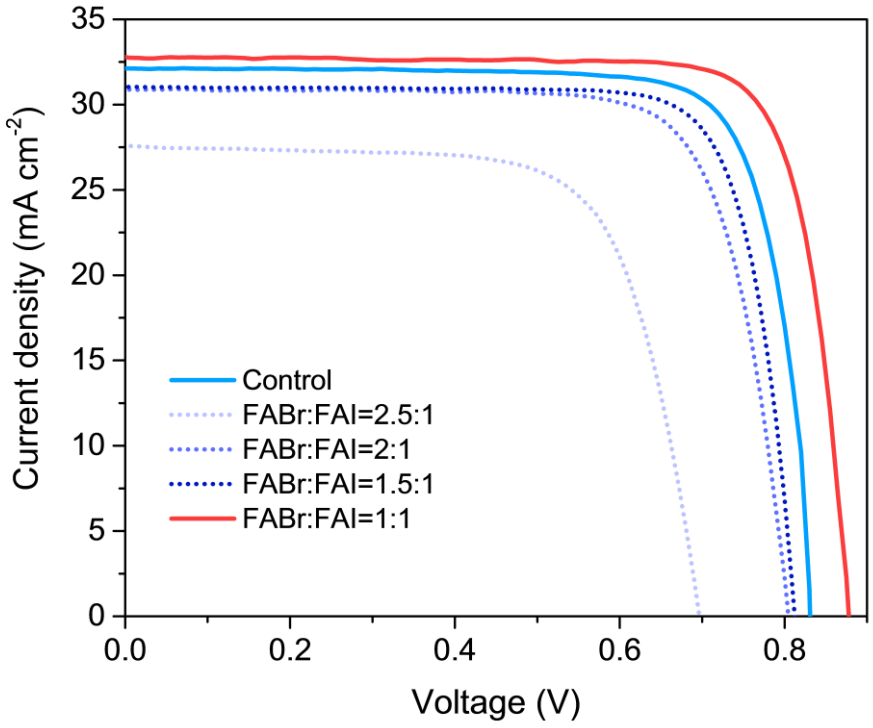

Supplementary Figure 4 | Performance of control and PHJ. The FL-WBG perovskite films with various content of FABr/FAI ions in the organic salt.

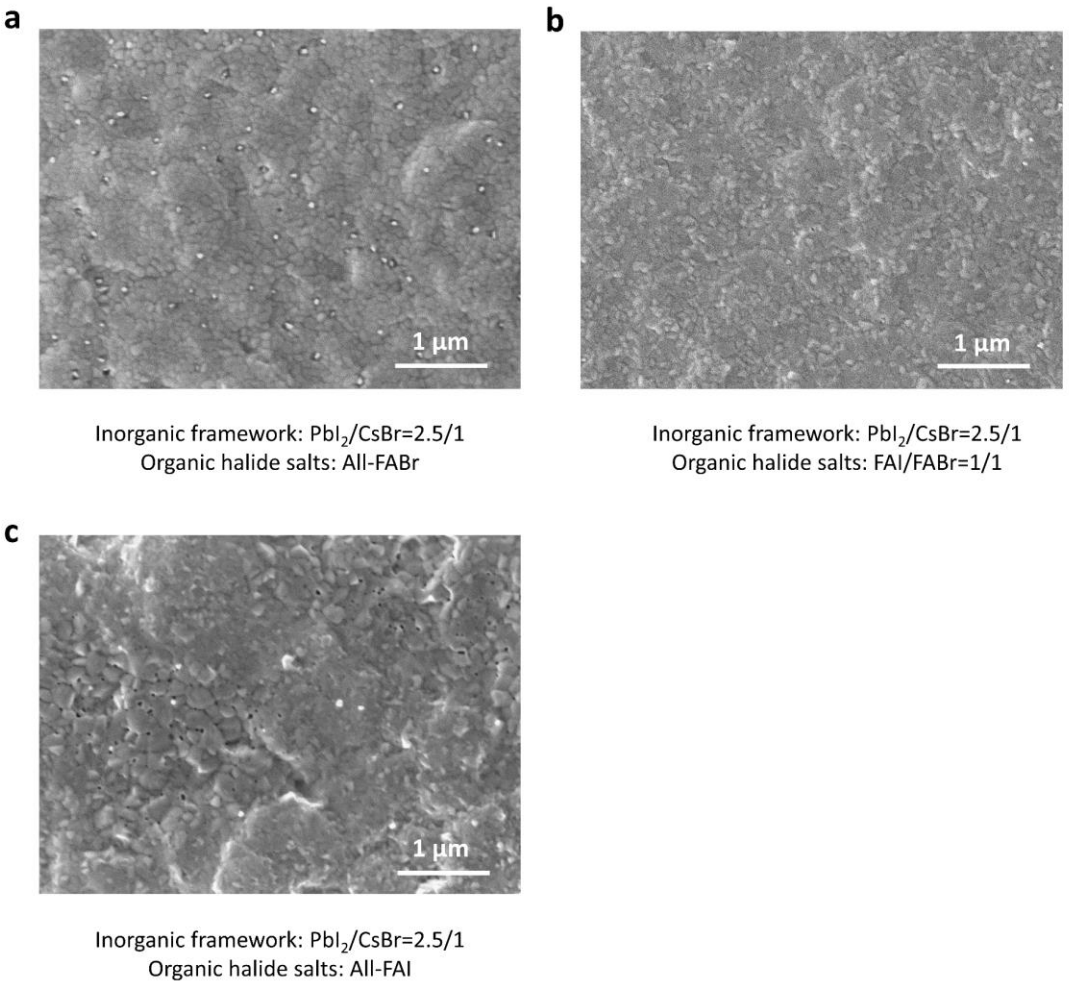

Supplementary Figure 5 | Top-view SEM image of FL-WBG perovskite films with various content of FAI/FABr in the organic salt. Organic halide salts: all-FABr (a), FAI/FABr= 1/1 (b) and all-FAI (c). PbI_2/CsBr inorganic layer of FL-WBG : PbI_2/CsBr= 2.5/1 (evaporation rate ratio).

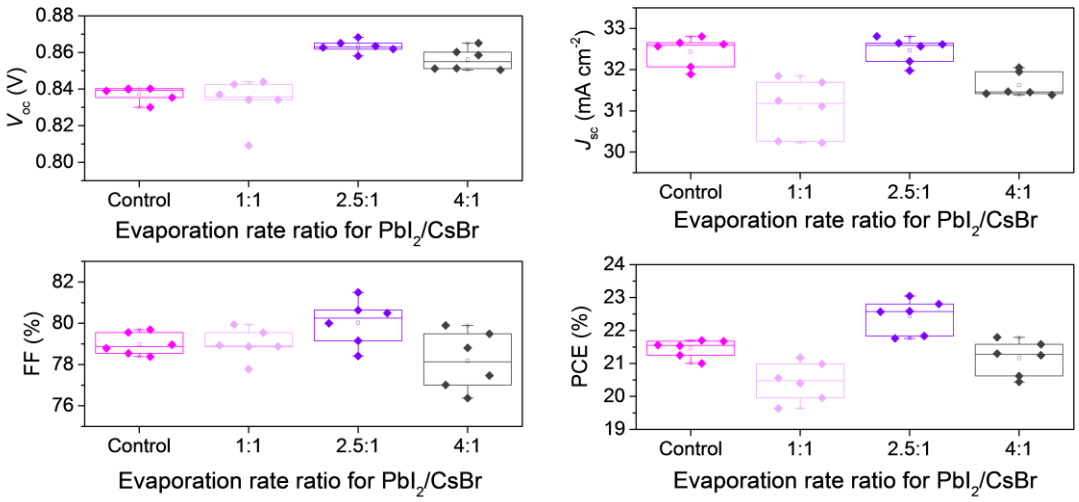

Supplementary Figure 6 | Performance of control and PHJ mixed Pb-Sn perovskite solar cells with various PbI_2/CsBr inorganic layer of FL-WBG.

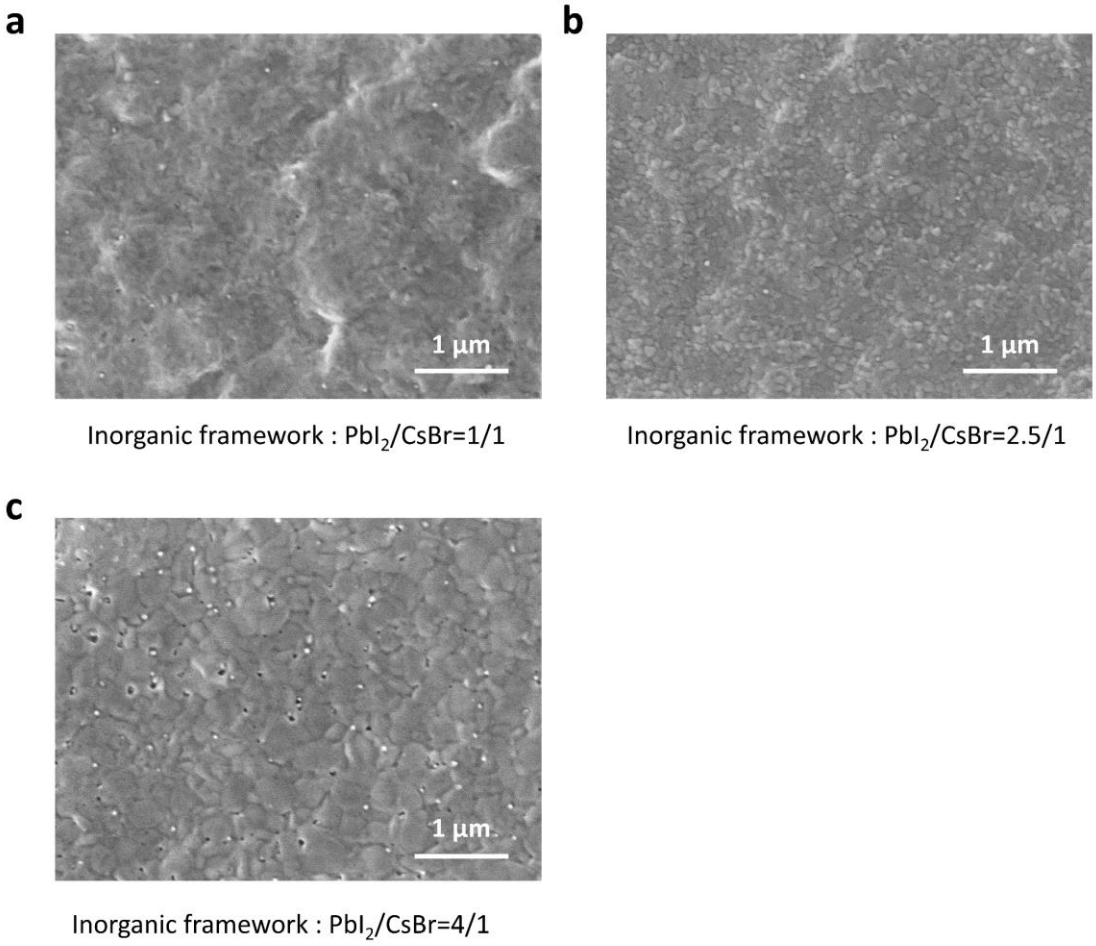

Supplementary Figure 7 | Top-view SEM image of FL-WBG perovskite films with various content of PbI_2/CsBr in the inorganic framework. Evaporation rate ratio: PbI_2/CsBr= 1/1 (a), 2.5/1 (b) and 4/1 (c). All Organic halide salts of FL-WBG: FAI/FABr= 1/1.

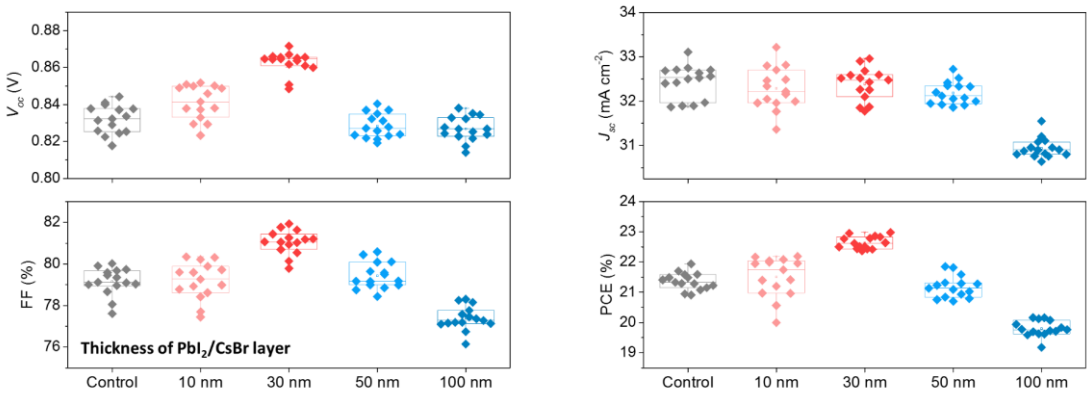

Supplementary Figure 8 | Performance of PHJ Pb-Sn perovskite solar cells with various thicknesses of the evaporated PbI_2/CsBr inorganic layer. Statistical performance of 15 devices for each type is presented. The optimal thickness of the evaporated PbI_2/CsBr inorganic layer is 30 nm, which is then transformed to 50-nm-thick FL-WBG perovskite layer after organic-salt treatment. The thickness of PbI_2/CsBr inorganic layer was read from the evaporation equipment (thickness was calibrated by evaporation of films on bare ITO glass substrate).

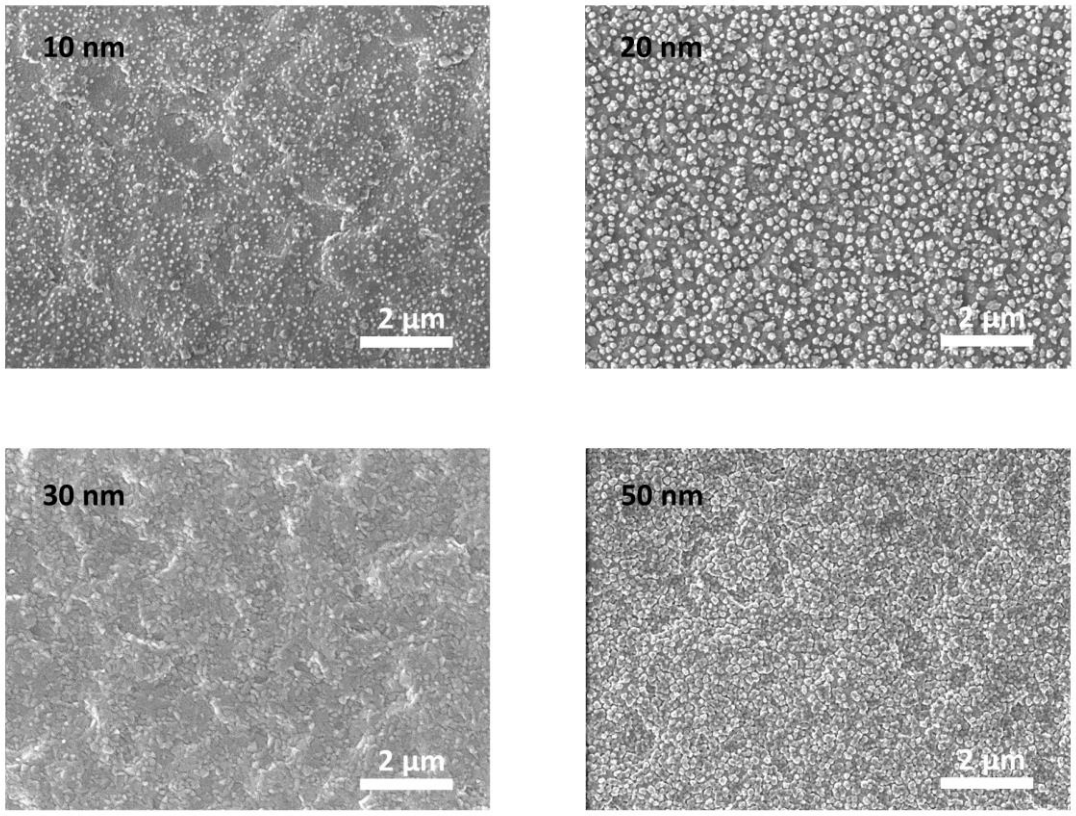

Supplementary Figure 9 | Top-view SEM images of PHJ Pb-Sn perovskite films with various thicknesses of the evaporated PbI_2/CsBr inorganic layer. The thickness of the FL-WBG perovskite layer is adjusted by the evaporated PbI_2/CsBr inorganic layer. When the thickness of PbI_2/CsBr inorganic layer is less than 30 nm, the resultant FL-WBG layer can't form a continuous and complete coverage on the bottom Pb-Sn perovskite film.

Supplementary Figs. 10-23

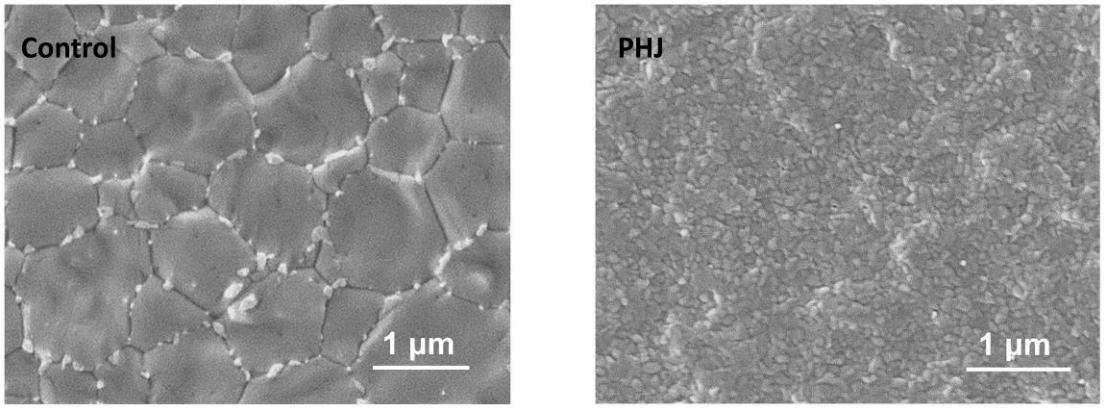

Supplementary Figure 10 | Top-view SEM of control and PHJ mixed Pb-Sn perovskite films.

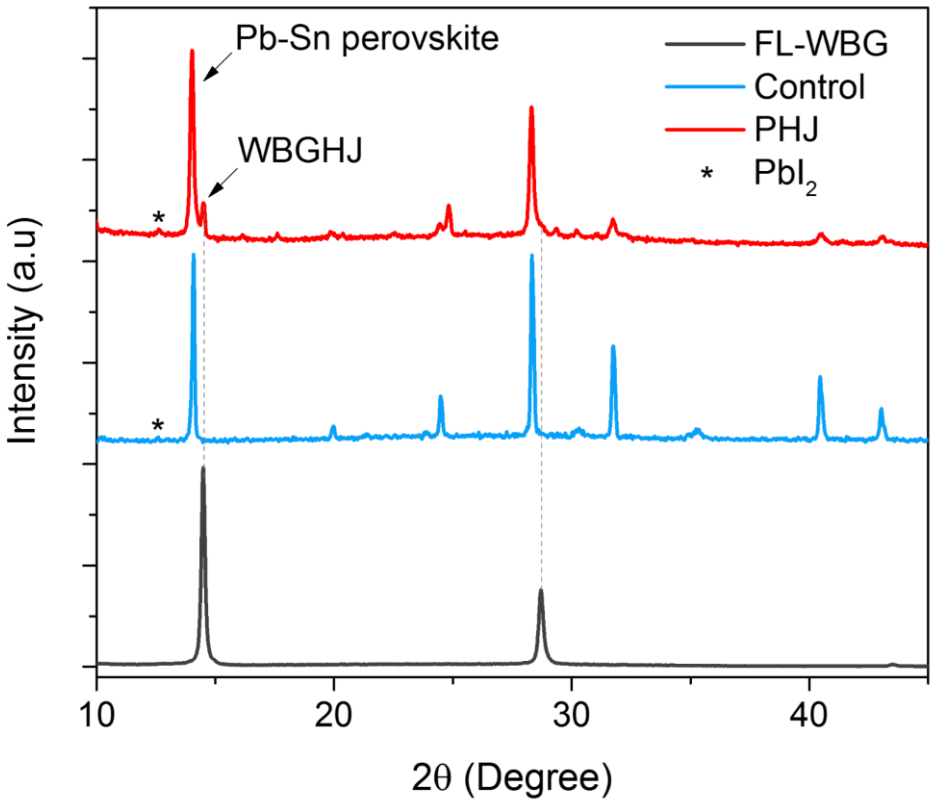

Supplementary Figure 11 | XRD patterns of bare FL-WBG perovskite film deposited on bare glass substrate (converted from 80 nm PbI_2/CsBr inorganic layer), control and PHJ Pb-Sn perovskite films.

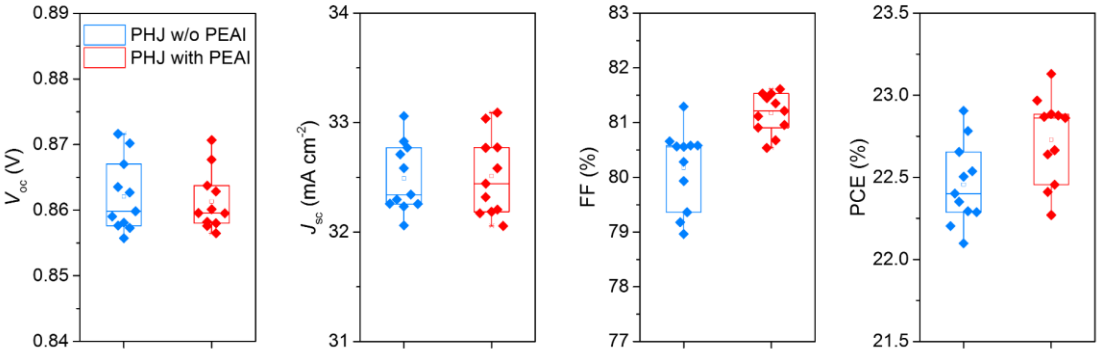

Supplementary Figure 12 | Performance of PHJ Pb-Sn PSCs with and without PEAI post-treatment. Comparison of photovoltaic performance between PHJ Pb-Sn PSCs with and without PEAI post-treatment fabricated over identical runs (11 devices for each type).

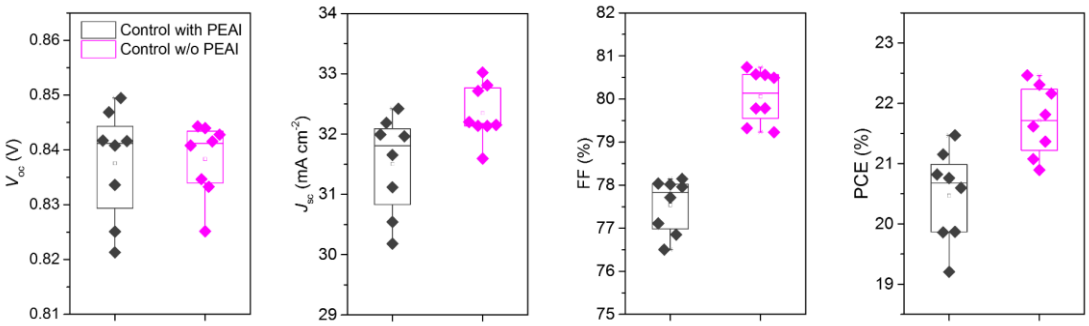

Supplementary Figure 13 | The photovoltaic performance of control Pb-Sn perovskite solar cell without and with PEAI post-treatment. Comparison of photovoltaic performance between control Pb-Sn PSCs with and without PEAI post-treatment fabricated over identical runs (8 devices for each type).

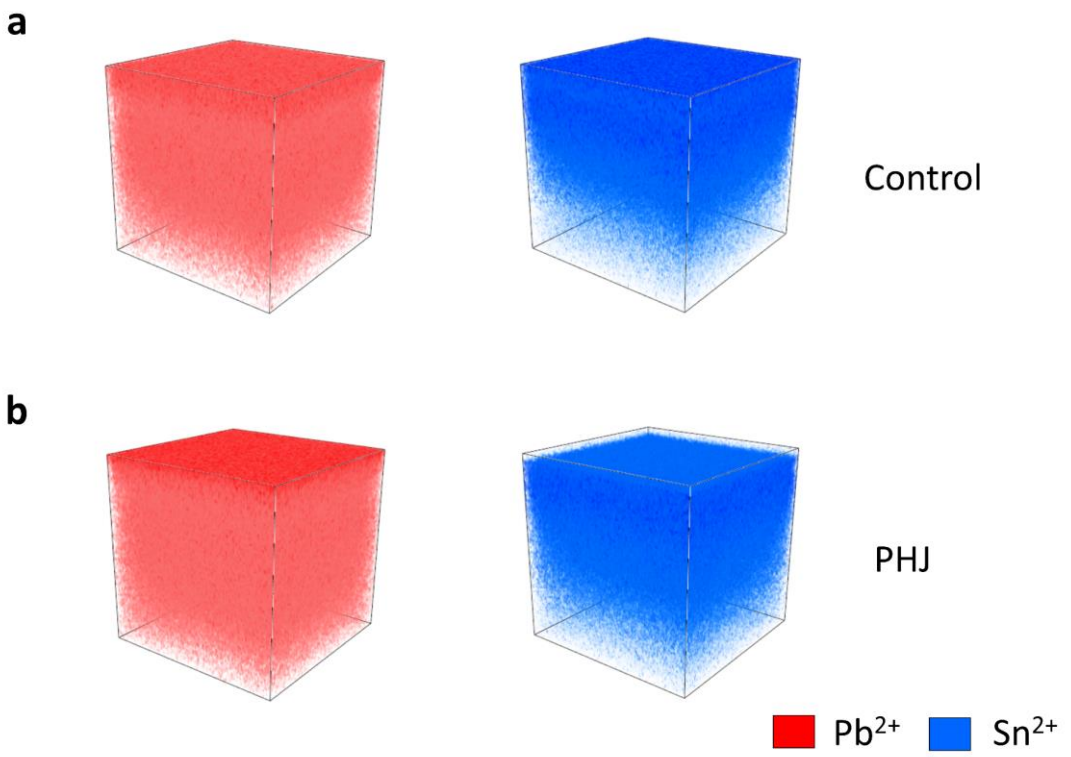

Supplementary Figure 14 | ToF-SIMS 3D maps of control and PHJ Pb-Sn perovskite film. Reconstructed, background subtracted 3D maps showing the distributions of Pb^{2+} and Sn^{2+} ions of narrow bandgap (a) control, (b) PHJ.

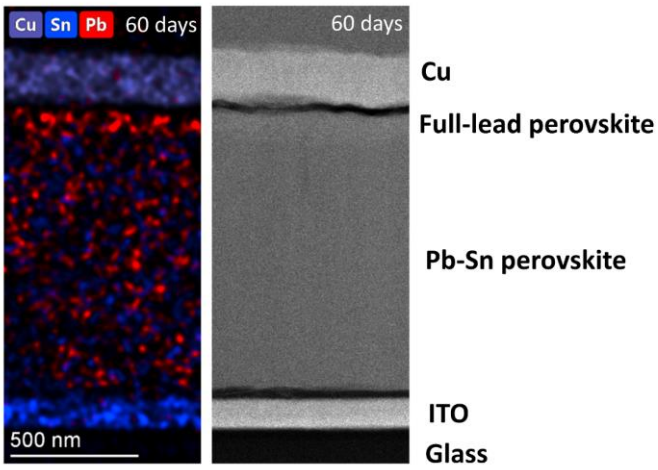

Supplementary Figure 15 | Cross-sectional HR-STEM image and the corresponding EDX mapping of PHJ narrow bandgap perovskite solar cells. The deceive storage in glovebox 60 days.

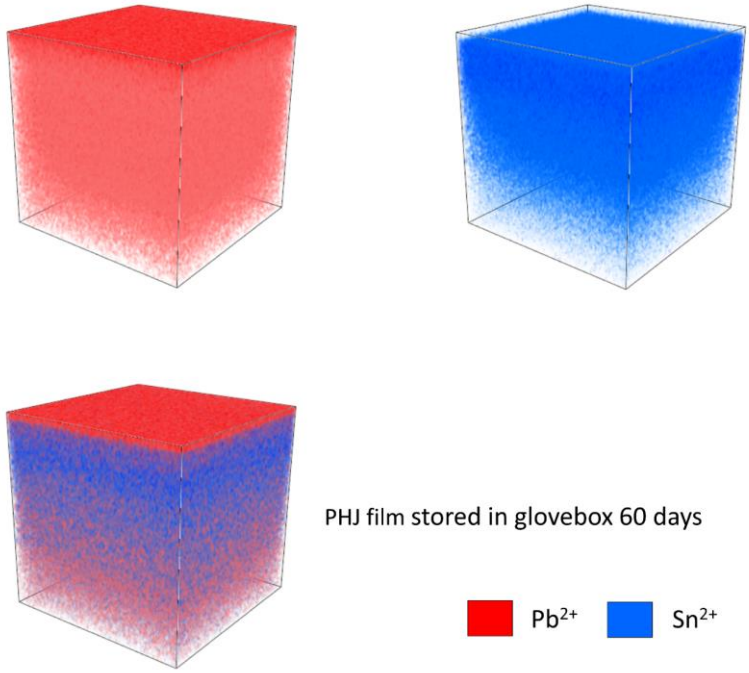

Supplementary Figure 16 | ToF-SIMS 3D maps of PHJ Pb-Sn perovskite film. Reconstructed, background subtracted 3D maps showing the distributions of Pb^{2+} and Sn^{2+} ions of PHJ Pb-Sn perovskite films storage in glovebox 60 days. The raster area of the primary ion beam was 100 μm×100 μm, and the thickness axis has been expanded for clarity.

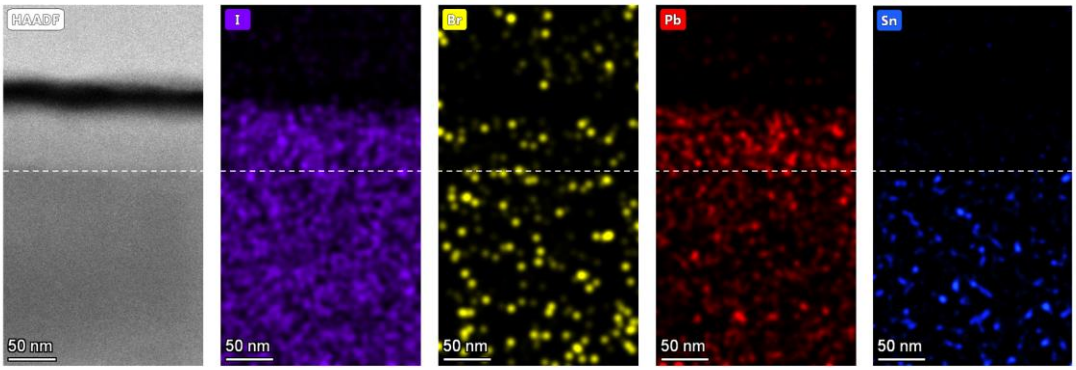

Supplementary Figure 17 | Cross-sectional HR-STEM image and the corresponding EDX mapping of narrow bandgap PHJ Pb-Sn perovskite solar cells.

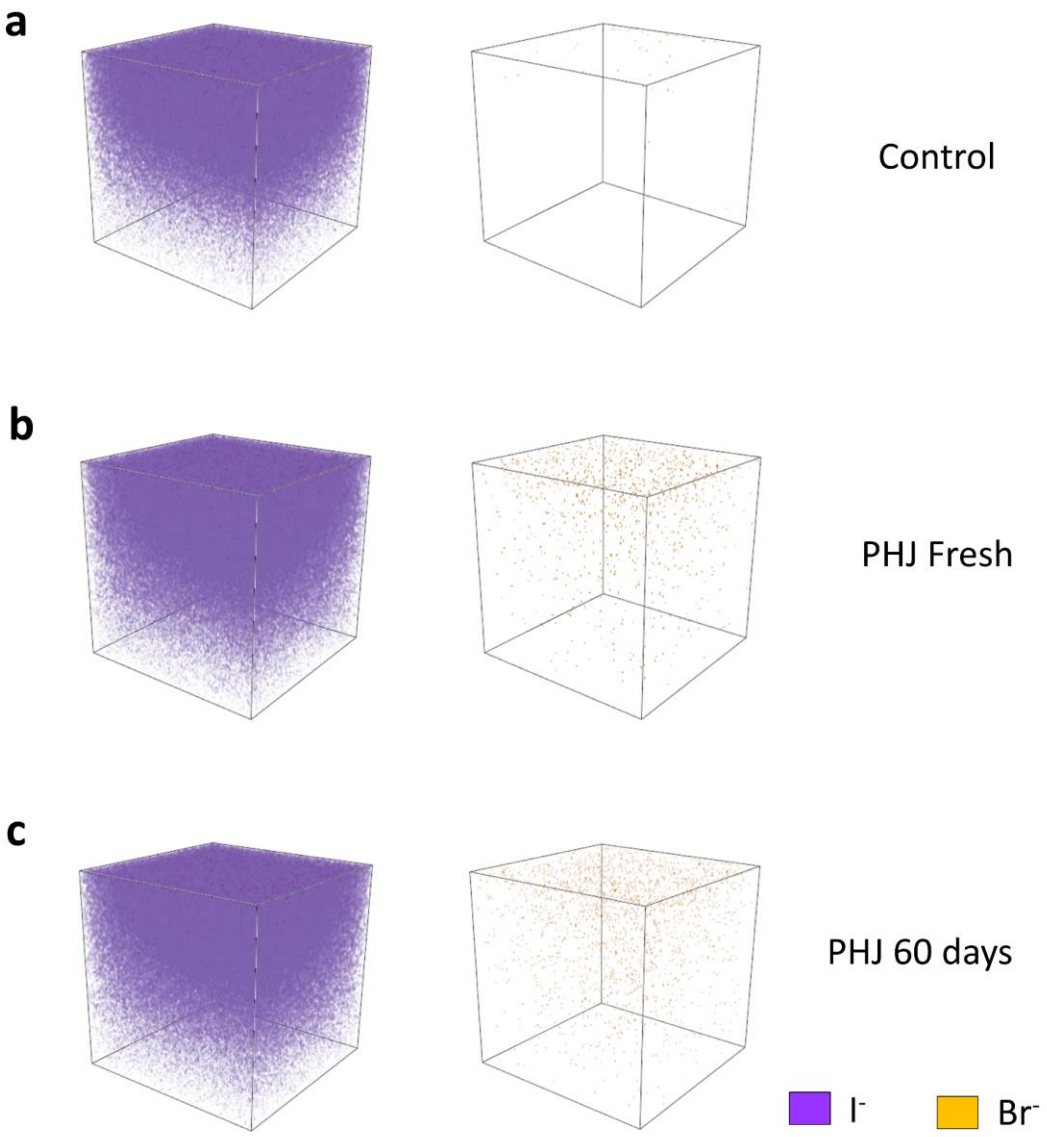

Supplementary Figure 18 | ToF-SIMS 3D maps of control and PHJ Pb-Sn perovskite film. Reconstructed, background subtracted 3D maps showing the distributions of I^- and Br^- ions of (a) control, (b) PHJ, (c) PHJ film storage in glovebox 60 days narrow bandgap perovskite films. The raster area of the primary ion beam was 100 μm×100 μm, and the thickness axis has been expanded for clarity.

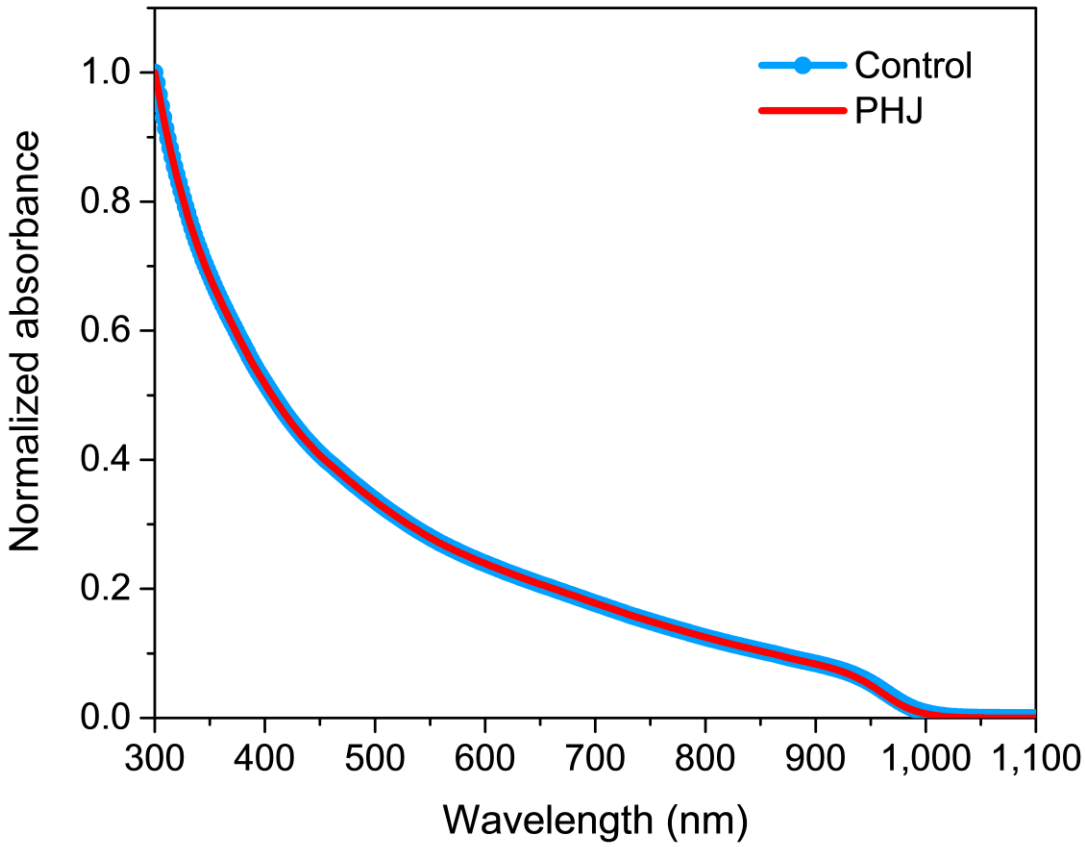

Supplementary Figure 19 | Absorption spectra of control and PHJ perovskite films.

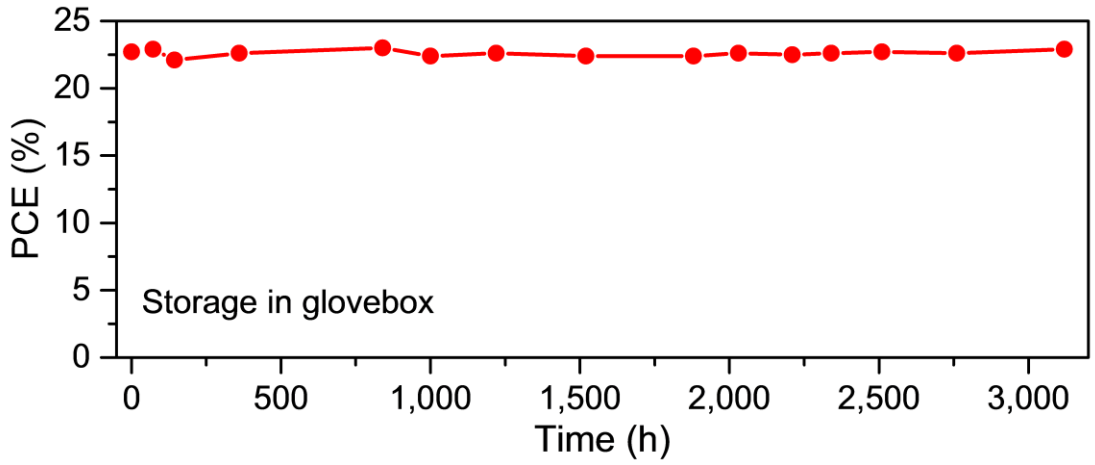

Supplementary Figure 20 | Shelf stability of PHJ Pb-Sn perovskite solar cells. The PHJ devices were stored under dark in the N_2 glovebox.

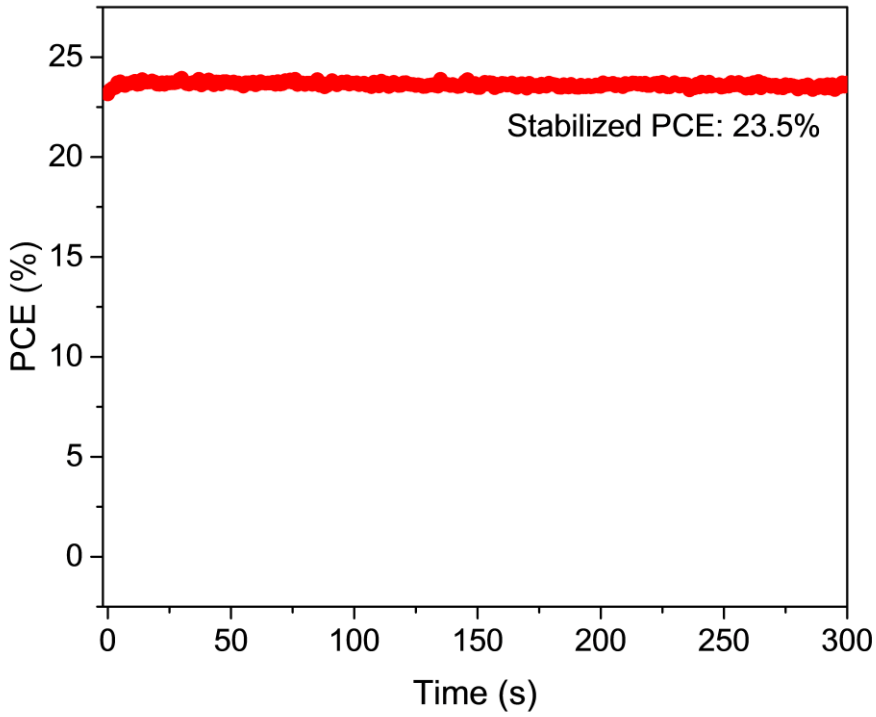

Supplementary Figure 21 | The steady-state PCE of the champion PHJ Pb-Sn perovskite solar cell.

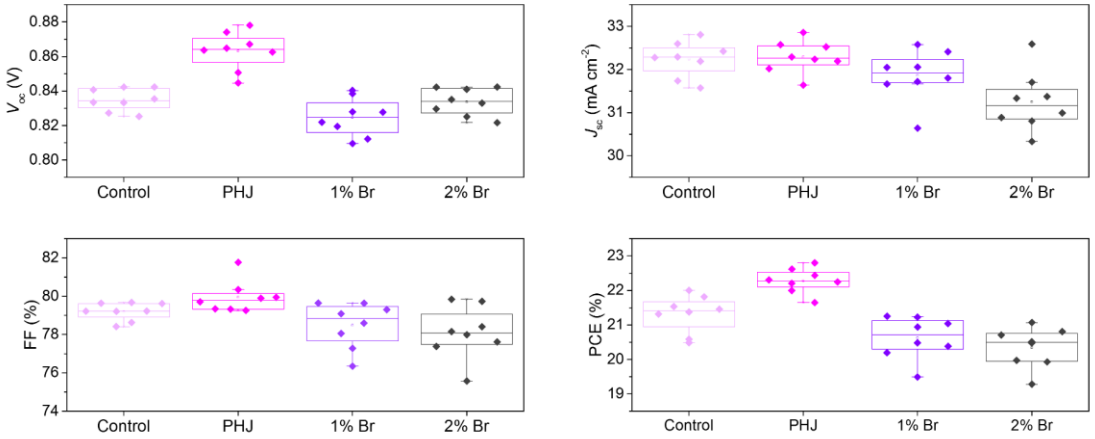

Supplementary Figure 22 | PV performance of Pb-Sn PSCs. PV performance of control and PHJ Pb-Sn narrow-bandgap perovskite solar cells, and control devices with 1% and 2% Br added.

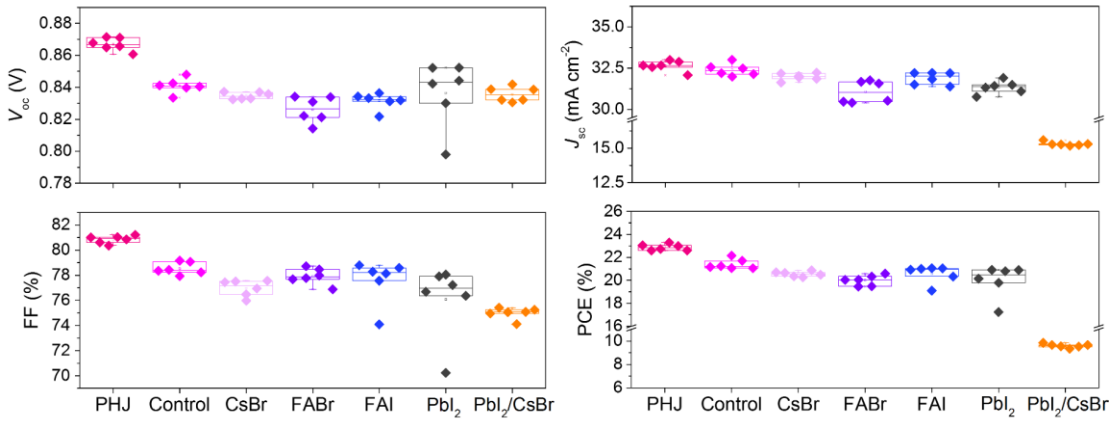

Supplementary Figure 23 | PV performance of PHJ, control and control with different passivation from materials of FL-WBG (6 devices for each type). FABr passivation: 80 µL FABr (0.5 mg mL^{-1} in IPA) was dynamically spin-coated on control Pb-Sn perovskite and heated at 100°C for 30 s; FAI passivation: 80 µL FAI (0.5 mg mL^{-1} in IPA) was dynamically spin-coated on control Pb-Sn perovskite and heated at 100°C for 30 s; CrBr passivation: 2 nm CsBr was deposited on control Pb-Sn perovskite by thermal evaporation; PbI_2 passivation: 2 nm PbI_2 was deposited on control Pb-Sn perovskite by thermal evaporation; PbI_2/CsBr passivation: 30 nm PbI_2/CsBr was deposited on control Pb-Sn perovskite by thermal evaporation. All passivation process was operated in N_2 glovebox.

Supplementary Note 2

Photovoltaic performance of Control and PHJ device with different ETL

PHJ PSCs with an ALD-SnO_2-based ETL performed similarly in PCE (23.2% vs 23.1%) compared to BCP-based devices (**Supplementary Fig. 24 and Supplementary Table 5**). Previous studies have demonstrated that better stability could be achieved by replacing BCP with ALD-SnO_2[1]. The unencapsulated PHJ solar cells exhibited excellent shelf-stability under storage in a N_2-filled glovebox; no obvious degradation in performance was observed after storage for over 3,000 h (**Supplementary Fig. 20**). We proceeded to investigate the atmospheric stability of mixed Pb-Sn perovskite solar cells with C_{60}/BCP or C_{60}/ALD-SnO_2 as the ETL (**Supplementary Fig. 25**). For both ETL structures, the PHJ devices showed better atmospheric stability than their control counterparts. Because of the protection provided by a robust ALD-SnO_2 film, the ALD-SnO_2-based PHJ devices demonstrated the best oxidation resistance, with no obvious degradation of their initial performance following 300 mins of air storage. This will allow the encapsulation of modules to be completed under ambient conditions, an approach that could reduce the fabrication costs compared to the encapsulation required in an inert environment.

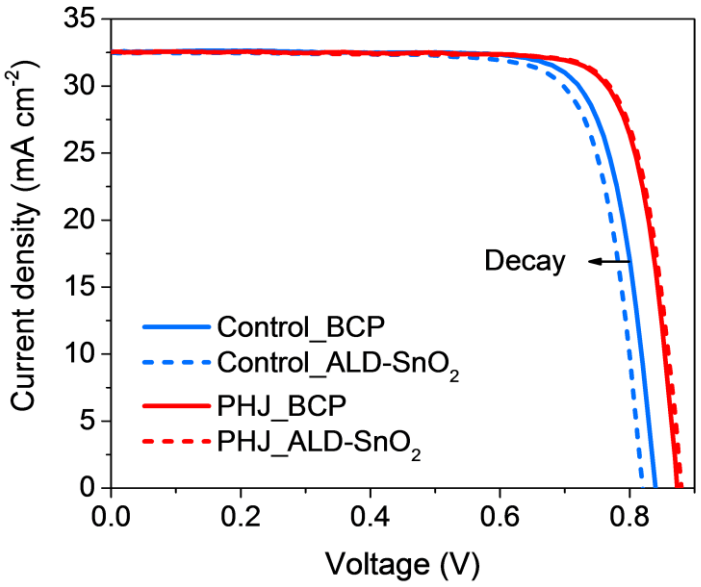

Supplementary Figure 24 | *J-V* curves of control and PHJ devices with absorber layer thicknesses of 1,200 nm. Control BCP: control Pb-Sn PSCs with C_{60}/BCP as the ETL; Control ALD-SnO_2: control Pb-Sn PSCs with C_{60}/ALD-SnO_2 as the ETL; PHJ BCP: PHJ Pb-Sn PSCs with C_{60}/BCP as the ETL; and PHJ ALD-SnO_2: heterojunction Pb-Sn PSCs with C_{60}/ALD-SnO_2 as the ETL. (Detailed parameters showing in **Supplementary Table 5**).

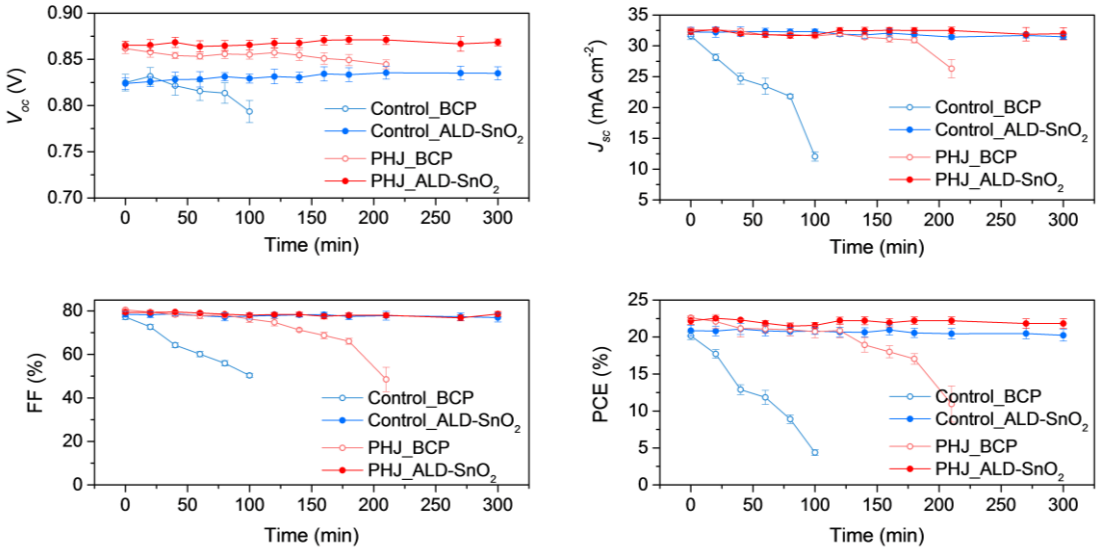

Supplementary Figure 25 | Atmospheric stability of Pb-Sn single junction solar cells stored in ambient air with a humidity <20%. The control devices exhibited fast degradation in performance after exposure to air. The PHJ samples showed much better tolerance to air exposure and could maintain their initial performance for the first 175 min. The device with ALD-SnO_2 showed much better tolerance to air exposure and PHJ ALD-SnO_2 device showed much better performance. The devices had a structure of Glass/ITO/PEDOT:PSS/perovskite/C_{60}/BCP or ALD-SnO_2/Cu.

Supplementary Fig. 26-35

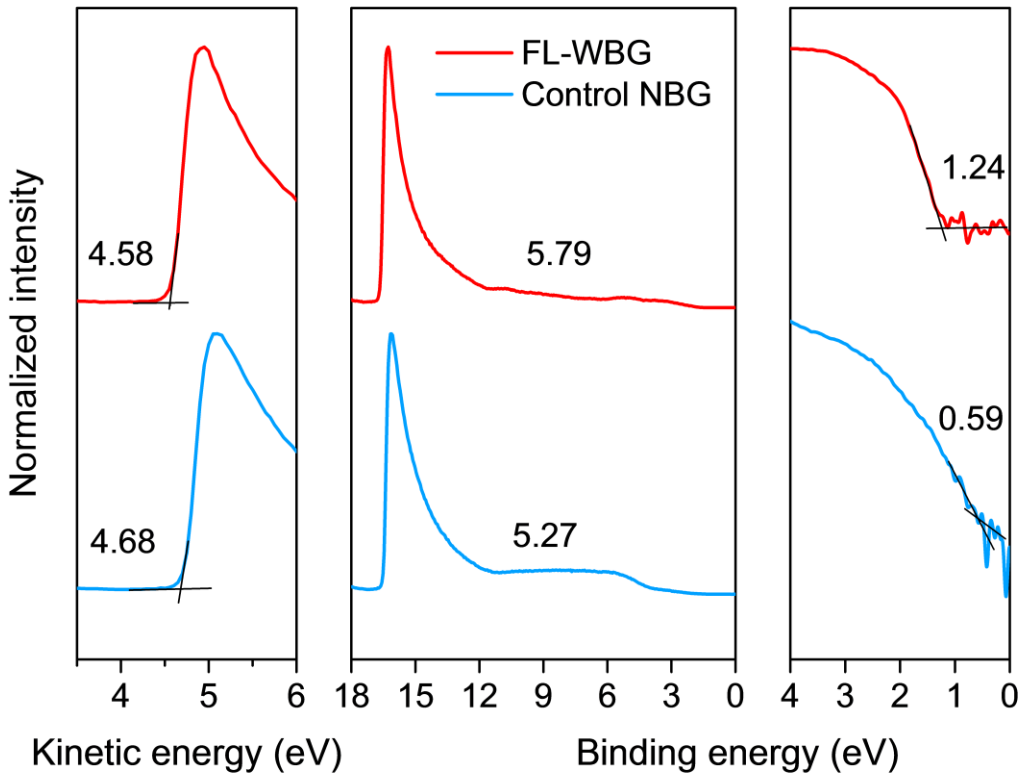

Supplementary Figure 26 | UPS of FL-WBG and control Pb-Sn perovskite films.

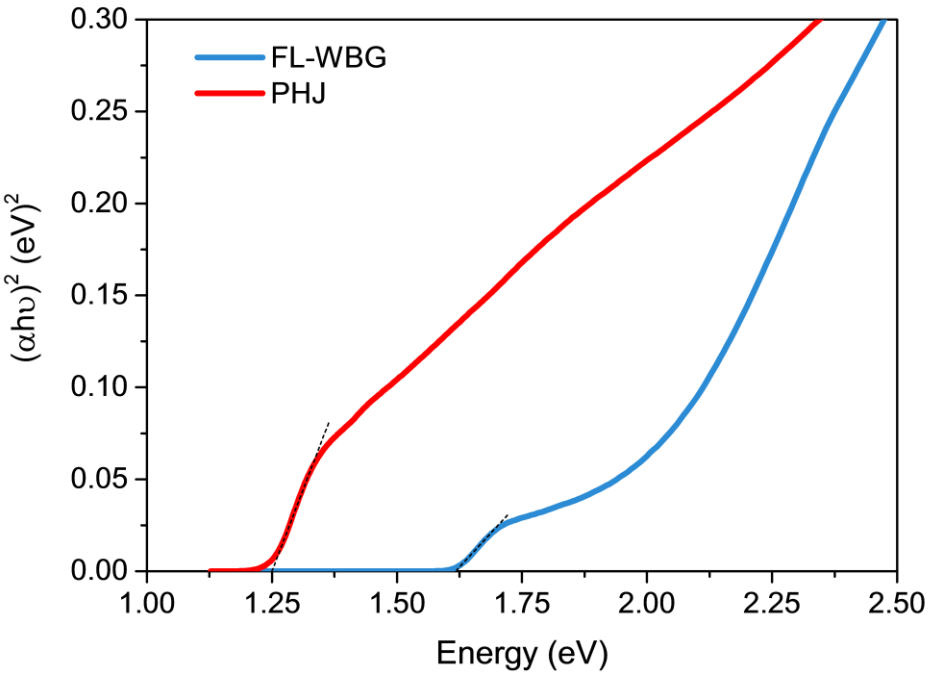

Supplementary Figure 27 | Calculated bandgap of FL-WBG and Pb-Sn perovskite films according to the absorption coefficient.

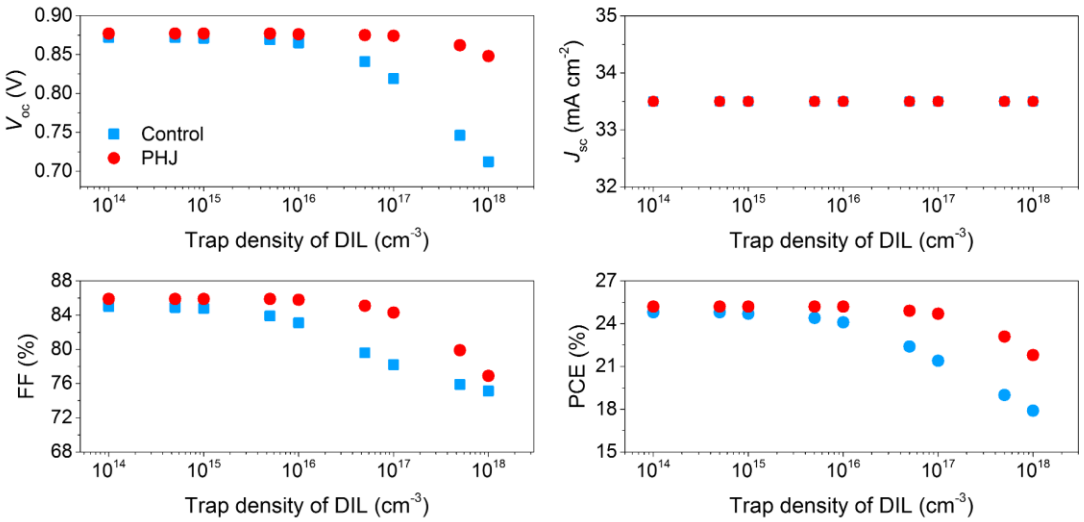

Supplementary Figure 28 | Simulated performance of the control and PHJ mixed Pb–Sn perovskite solar cells with IDL for different trap densities. The parameters of the simulation were set to be identical with **Supplementary Tables 4-5**. Solar Cell Capacitance Simulator (SCAPS 1D) tool (version 3.3.10, ELIS, University of Gent, Belgium) is used as the platform for the simulation of NBG perovskite solar cell.

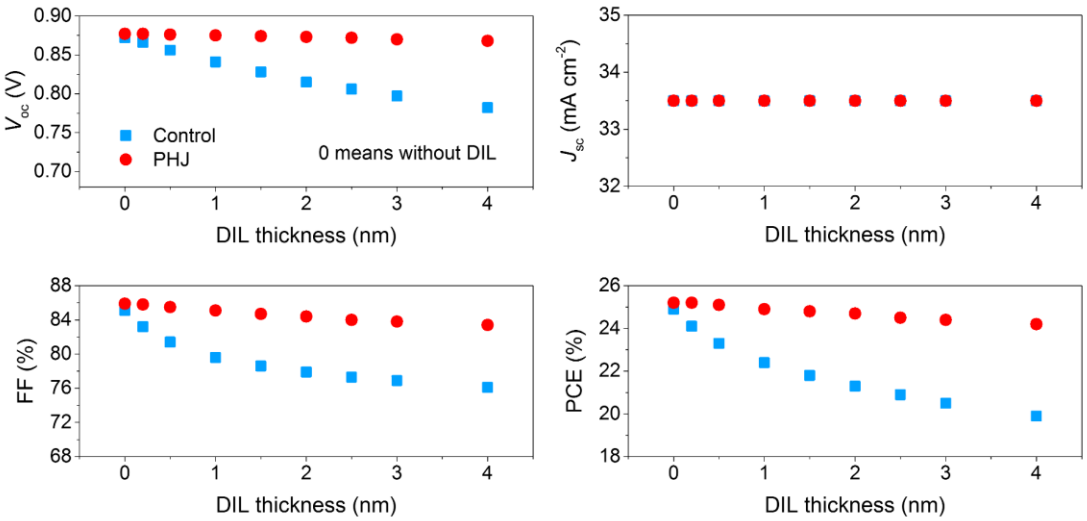

Supplementary Figure 29 | Simulated performance of the control and PHJ mixed Pb–Sn perovskite solar cells with different thickness DIL. The parameters of the simulation were set to be identical with **Supplementary Tables 6-7**. Solar Cell Capacitance Simulator (SCAPS 1D) tool (version 3.3.10, ELIS, University of Gent, Belgium) is used as the platform for the simulation of NBG perovskite solar cell.

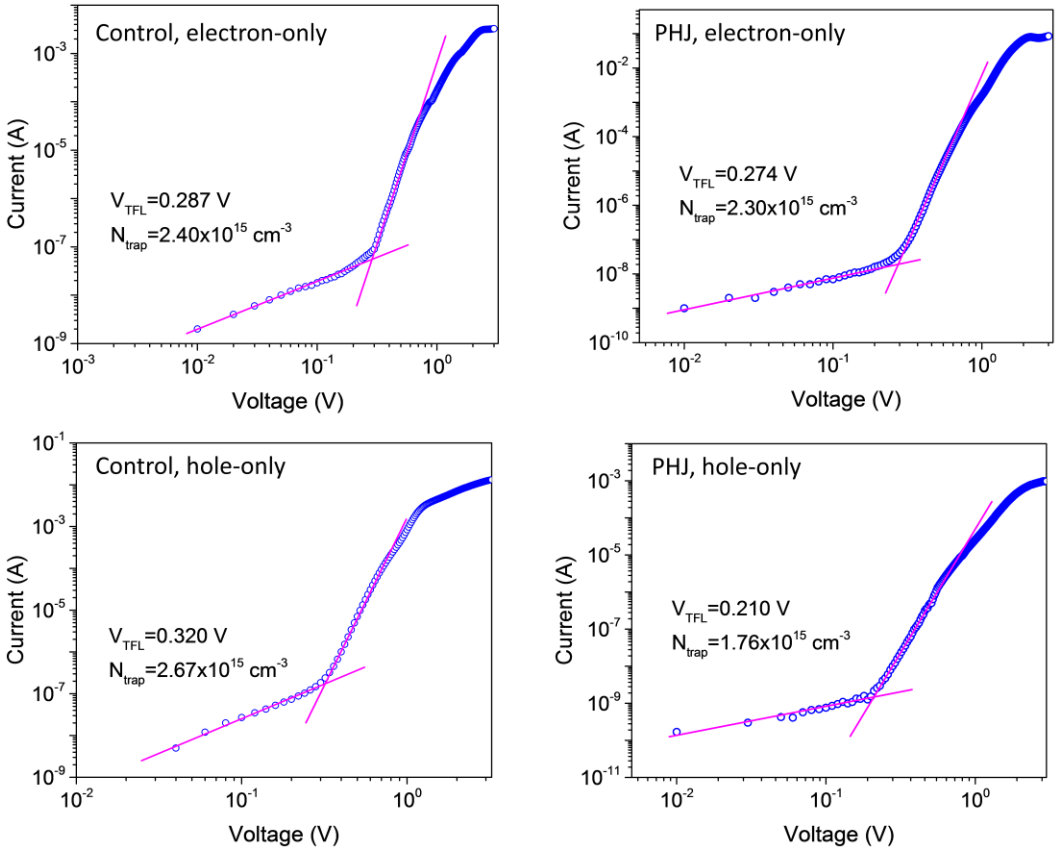

Supplementary Figure 30 | Current-voltage traces and trap density of Pb-Sn low-bandgap perovskites as determined by the space-charge-limited current (SCLC) method. Electron-only and hole-only device structures were constructed to obtain the electron trap density and hole trap density, respectively. The trap density N_{trap} is determined by the equation: $V_{TFL}=qN_{trap}L^2/(2\varepsilon\varepsilon_0)$, where V_{TFL} is trap-filled limit voltage, L is the thickness of perovskite film, ε is the relative dielectric constant of perovskite, and ε_0 is the vacuum permittivity.

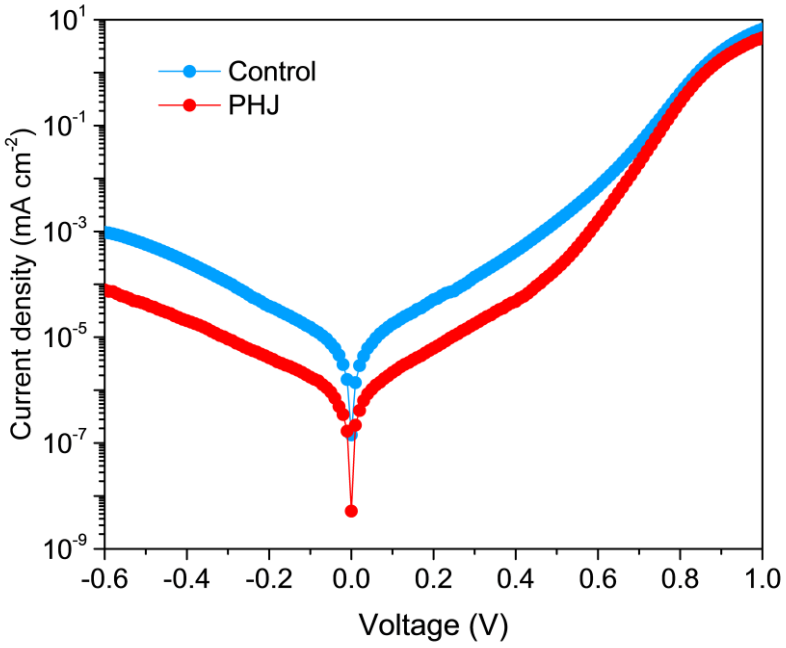

Supplementary Figure 31 | Dark *J-V* curves of the control and PHJ Pb-Sn perovskite devices.

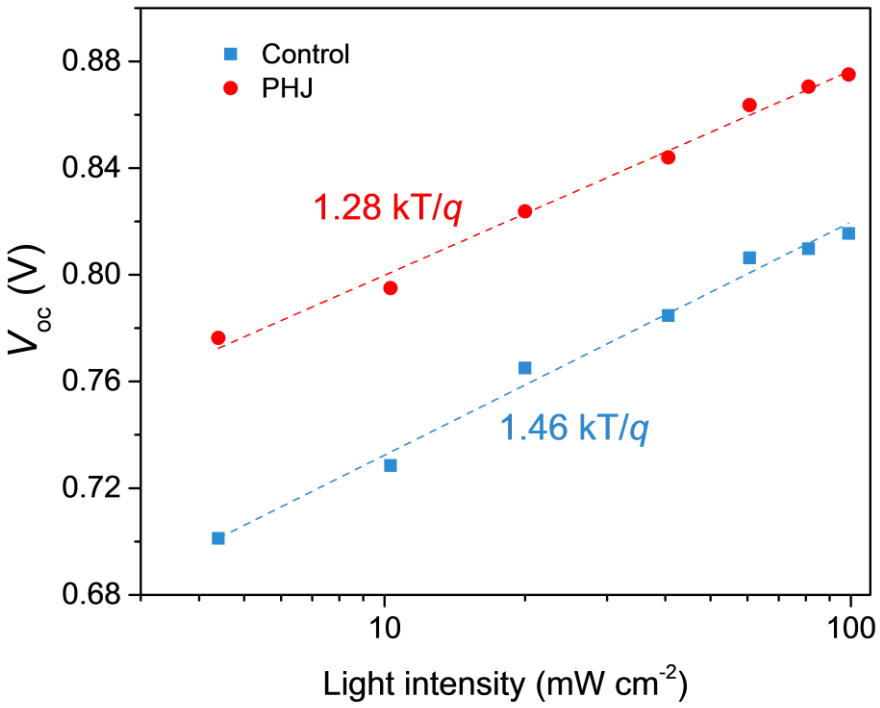

Supplementary Figure 32 | The correlation between V_{oc} and light intensity of control and PHJ narrow-bandgap perovskite solar cells.

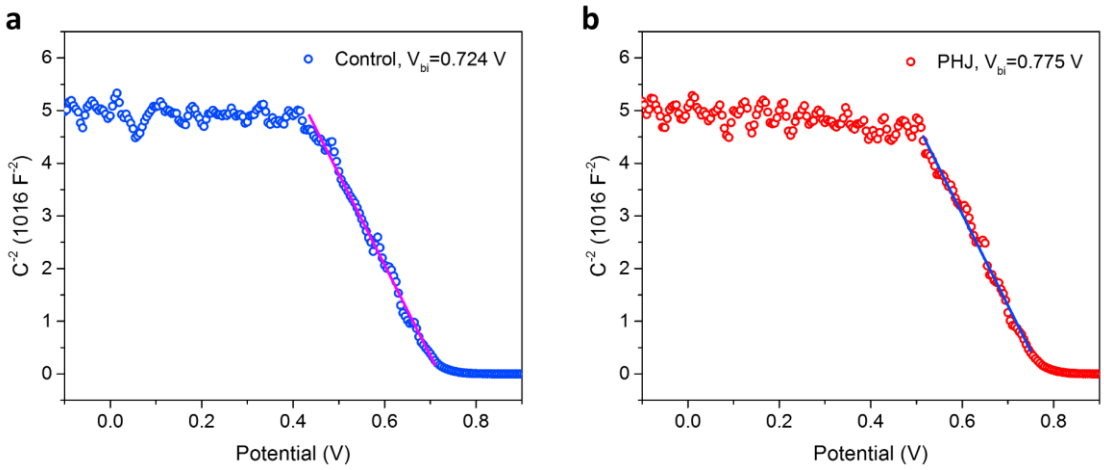

Supplementary Figure 33 | Mott-Schottky curve of control and PHJ Pb-Sn PSCs. Mott-Schottky (M-S) plot analysis from capacitance-voltage measurements for mixed Pb-Sn narrow-bandgap perovskite solar cells at 10 kHz under dark condition. The built-in potential (V_{bi}) is calculated according to the equation: V_{bi} = -y/k; where y is the intercept of Y-axis, k is the slope of fit line. The calculated V_{bi} were 0.724 and 0.775 V for control (a) and PHJ (b) devices, respectively.

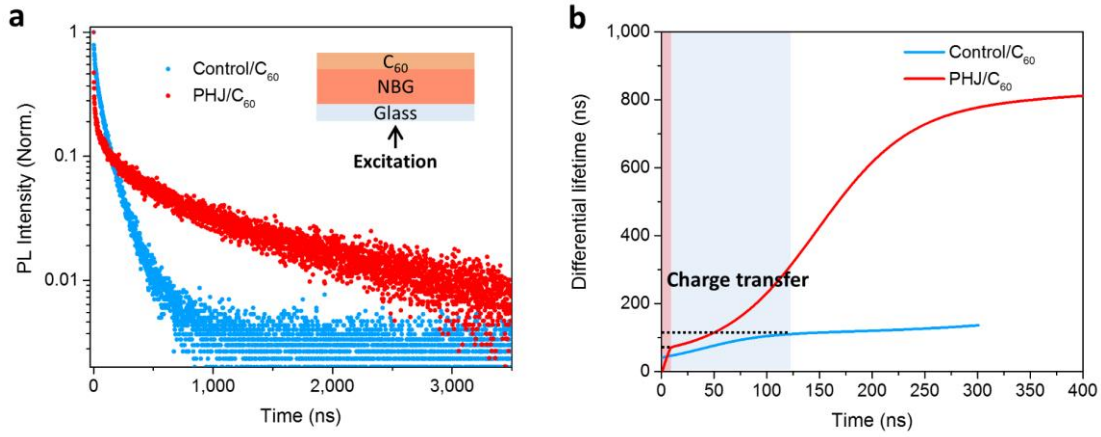

Supplementary Figure 34 | Differential lifetime of control and PHJ film. a, Time-resolved PL of control and PHJ perovskite films with C_{60} on bare glass substrates. A red laser diode ($\lambda = 630$ nm) was used for the excitation source. **b,** Computed differential lifetimes of control/C_{60} and PHJ/C_{60} film from fits to the transients in (a).

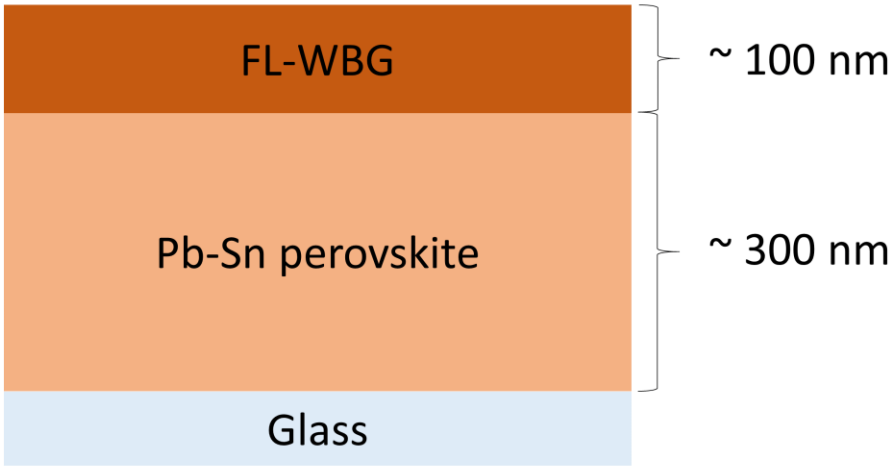

Supplementary Figure 35 | The structure schematic of 3D/3D bilayer PHJ perovskite film for TA.

Supplementary Note 3

Optical and electrical models useing GenPro4 smilucation tools

Optical model

In the thin-film optical system of the all-perovskite tandem solar cell, the implied photocurrent (J_{ph}) of each layer can be calculated by the net-radiation method, which has been explained elsewhere[2]. By adjusting the thicknesses of WGB and NGB perovskite layers, a matched J_{ph} (16.54 mA cm^{-2}) can be reached between two subcells, resulting in an optimized PCE in an assumed scenario where two subcells have similar FFs.

Electrical model

The *J-V* curve of single-junction solar cells can be reproduced by the two-diode model of the solar cell. An equivalent electrical circuit of the solar cell is defined by seven parameters, which can be extracted by fitting *J-V* curves of single-junction cells (**Supplementary Figs. 36a, b**) using a Nelder-Mead simplex algorithm[3]. The equivalent electrical circuit of the tandem solar cell, which is a series connection of two single-junction models, can be represented using the fit parameters. Here we use two NGB and three WGB solar cells to build six tandem combinations. The *J-V* curves of six tandem solar cells are shown in **Supplementary Fig. 36c**. PV performance of single-junction and tandem solar cells are listed in **Supplementary Table 12**.

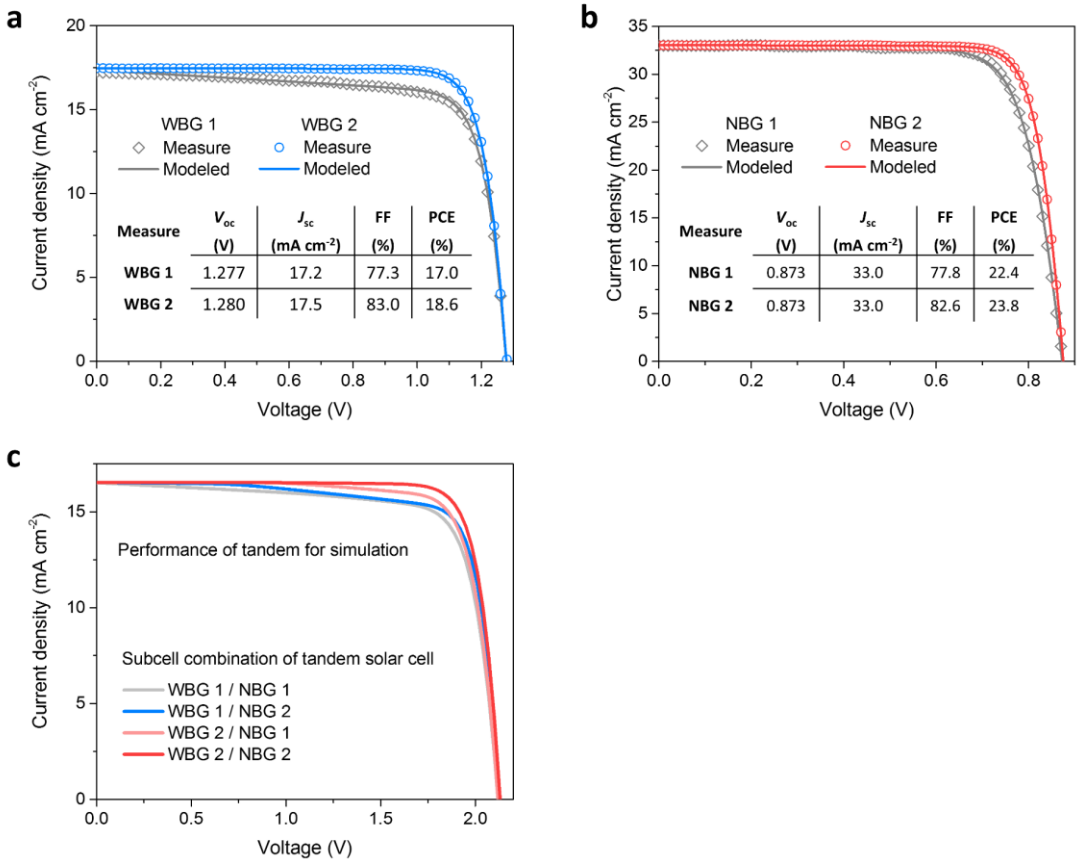

Supplementary Figure 36 | Measured and modeled *J-V* curves of single and tandem solar cell. a-b, measured and modeled *J-V* curves of single-junction WBG (a) and NBG (b) perovskite solar cells. **c,** Photovoltaic performance of tandem solar cells with different WBG and NBG subcell combination for simulation (the photovoltaic performance parameter shown in **Supplementary Table 12**).

Supplementary Figs. 37-42

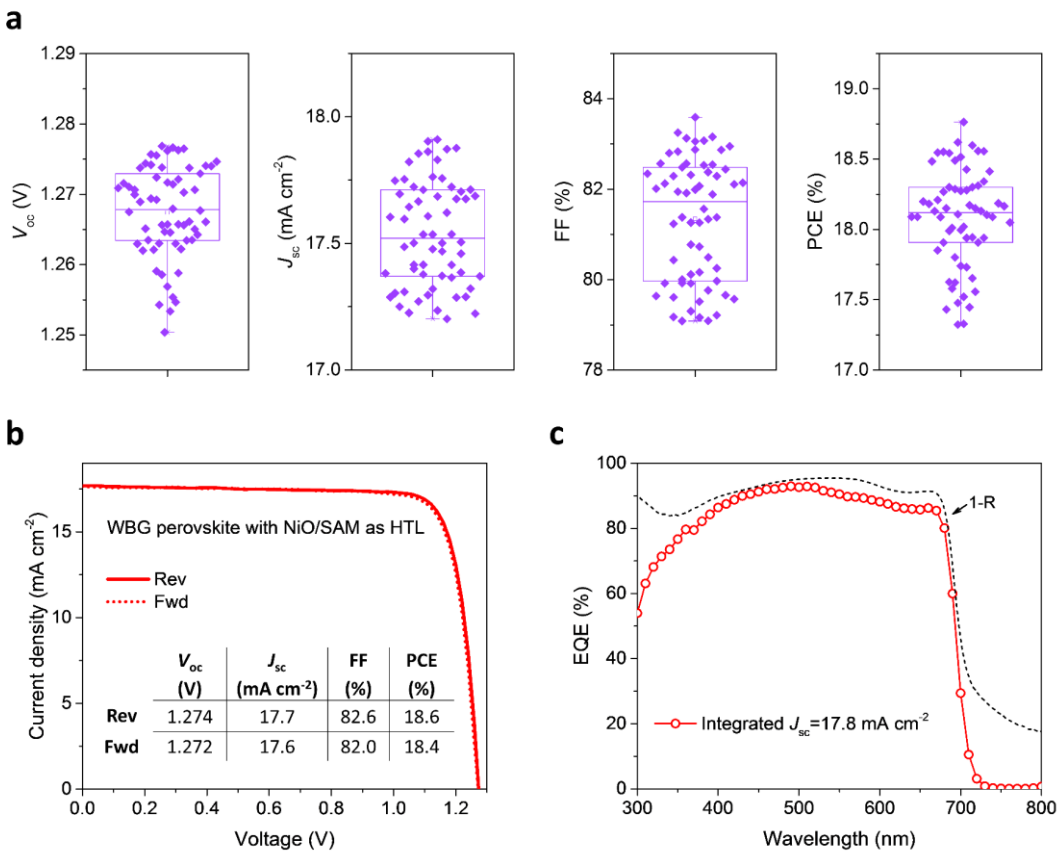

Supplementary Figure 37 | Photovoltaic performance of wide-bandgap perovskite solar cells. a, Statistics of PV parameters among 62 devices. **b-c,** *J-V*, EQE and total absorptance (1-R) curves of the best-performing WBG device.

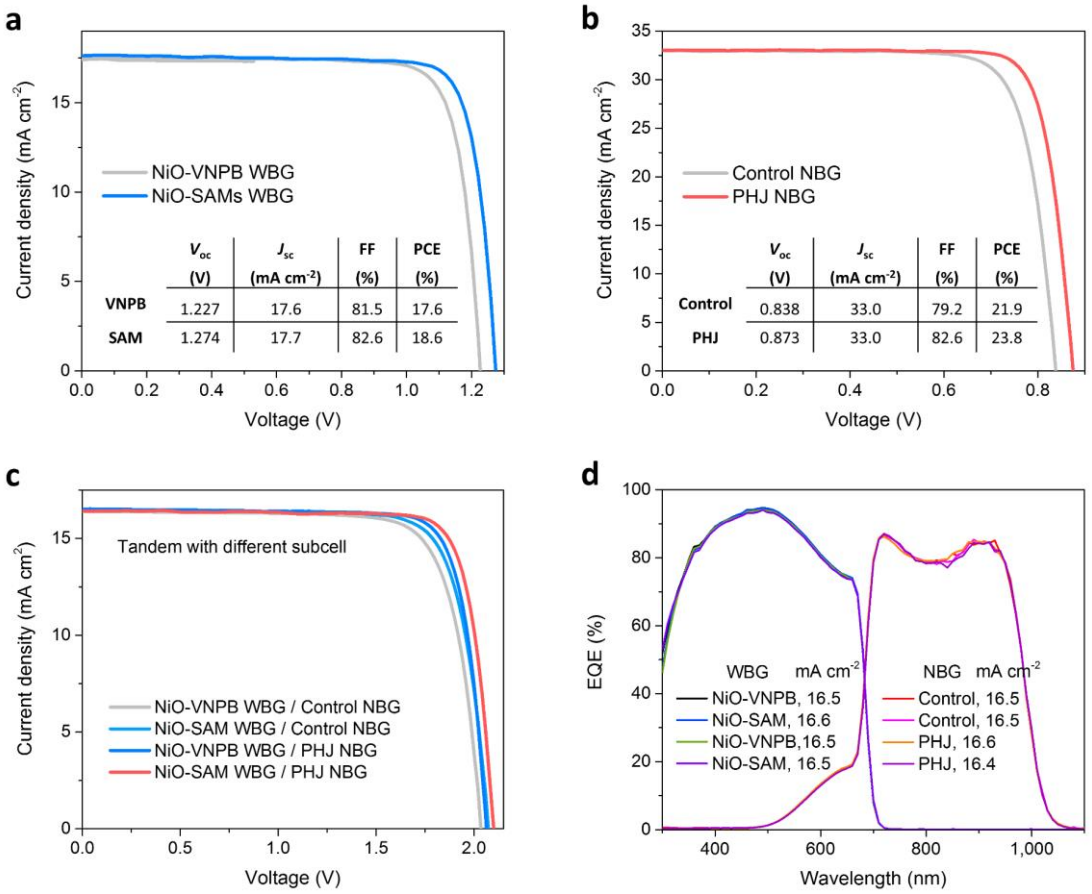

Supplementary Figure 38 | Photovoltaic performance of WBG, NBG subcell and tandem solar cells. a, *J-V* curves of wide-bandgap PSCs with bare VNPB and SAM modified NiO as the HTL. **b,** *J-V* curves of control and PHJ narrow-bandgap PSCs. **c-d,** *J-V* and EQE curves of tandem solar cell with different subcells. The integrated J_{sc} values of WBG and NBG subcells from EQE spectra shows that there is an agreeing well current density matching between the subcells for different tandem solar cells (the photovoltaic performance parameter shown in **Supplementary Table 13**).

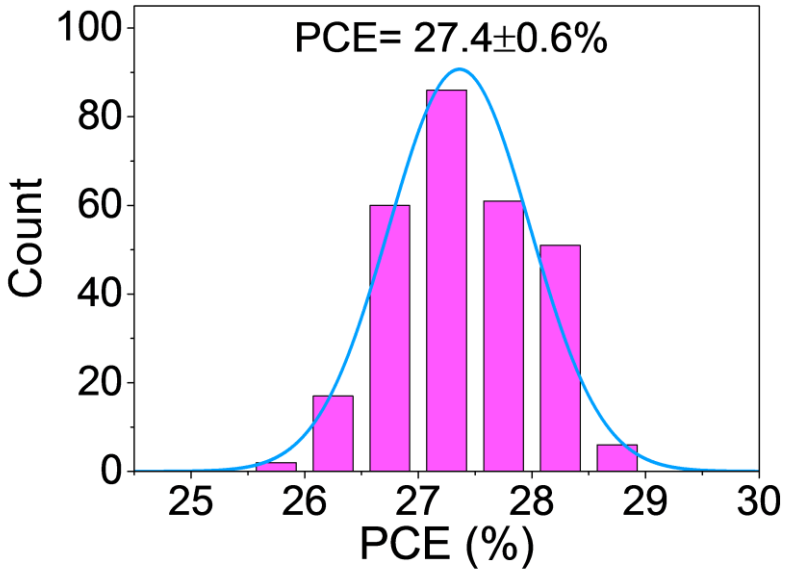

Supplementary Figure 39 | the performance of PHJ tandem solar cells. The PCE distribution of PHJ tandem devices (282 devices), showing an average PCE of 27.4±0.6% (aperture area 0.049 cm^2).

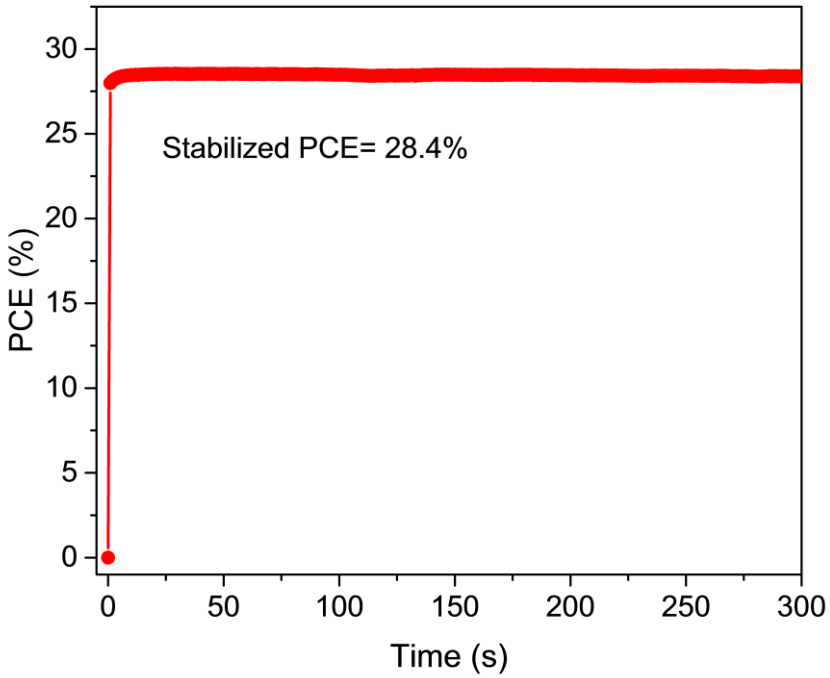

Supplementary Figure 40 | The steady-state PCE of the PHJ champion tandem device. The device aperture area is 0.049 cm^2.

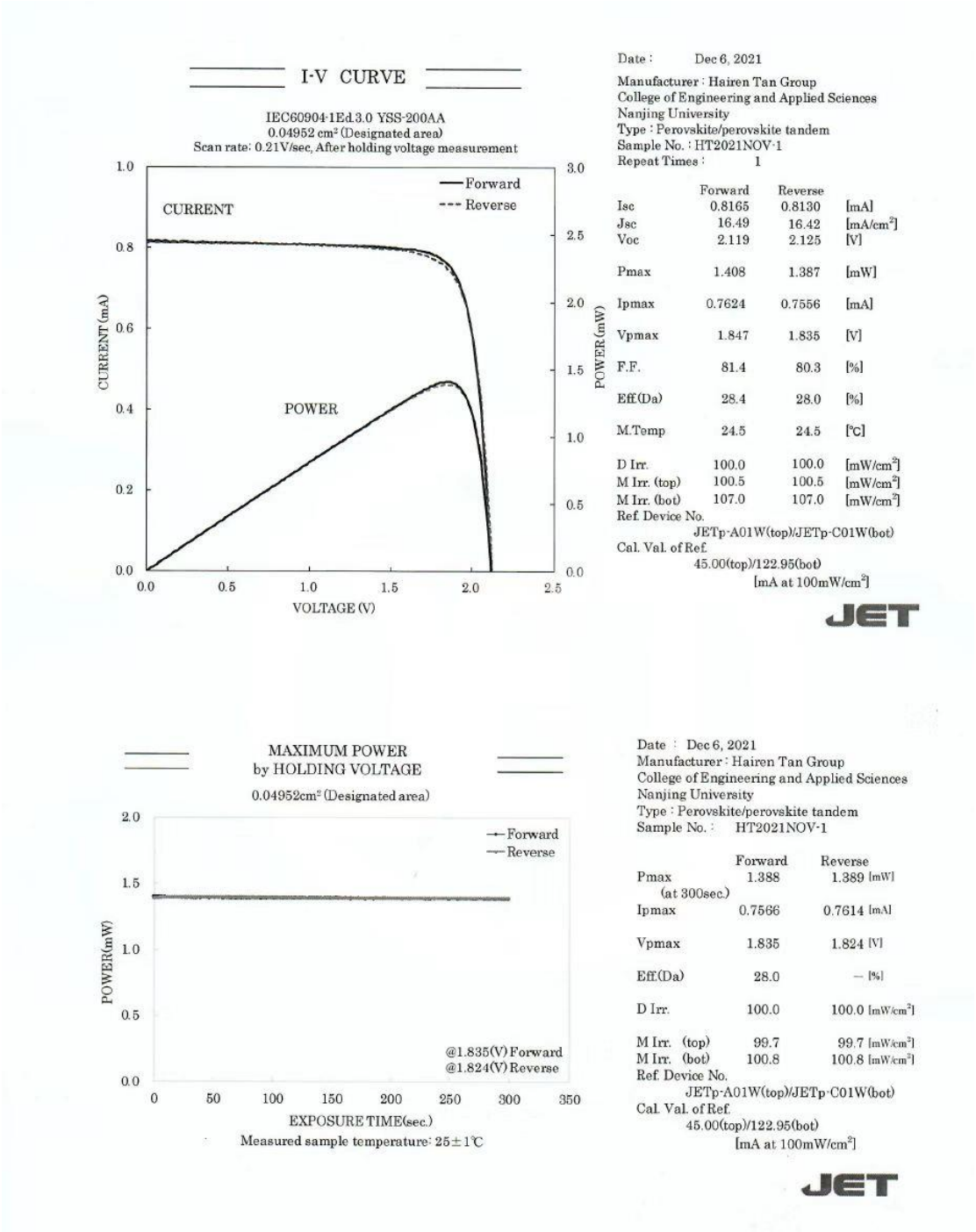

Supplementary Figure 41 | Certified results of all-perovskite tandem solar cell with PHJ. The devices delivered certified stabilized PCEs of 28.0%.

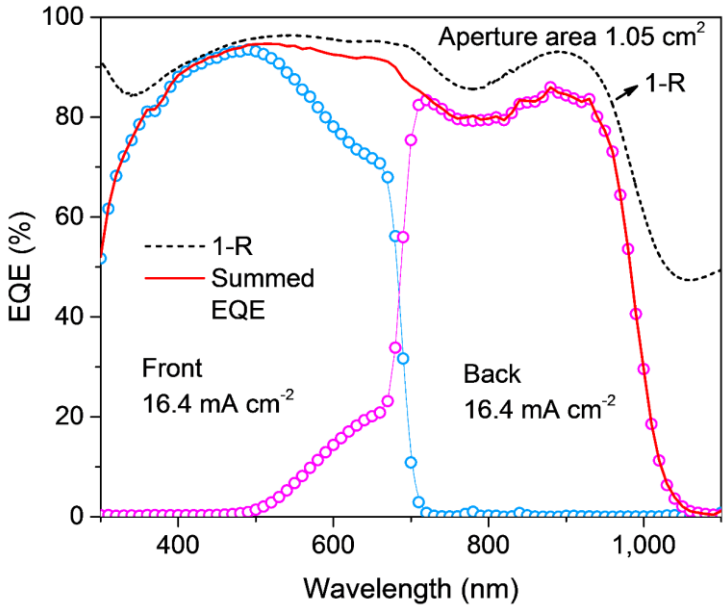

Supplementary Figure 42 | EQE spectra and absorptance (1-R) of large-area tandem solar cell. The device aperture area is 1.05 cm^2.

Supplementary Note 4

Electrical losses

The electrical losses in all-perovskite tandem solar cell includes subcell open-circuit voltage loss, tunnel recombination junction additional interfacial recombination loss and FF loss.

Subcell open-circuit voltage and FF loss:

Comparing the Shockley-Queisser limit based on detailed balance considerations[4] , the $V_{oc}/V_{oc,SQ}$ ratios of WBG and NBG sub-cells are ~0.85 and ~0.9, respectively. In addition, FF/FF_{SQ} ratios of WBG and NBG sub-cells are ~0.91 and ~0.93, respectively.

The subcell V_{oc} loss is mainly due to the non-radiative recombination in perovskite bulk and perovskite/ transport layer interface. Developing interfacial passivation and bulk additives to reduce defect density will be the main strategy boosting potential V_{oc}. FF loss is mainly due to charge carrier transport losses and thus induced recombination losses [5]. Therefore, more suitable charge carrier transport materials and methods of reducing defect density need to be explored in the future.

Tunnel recombination junction additional interfacial recombination loss:

The interconnection of WBG and NBG subcells in tandem can lead to significant additional Voc deficit due to additional interfacial recombination induced by the Tunnel recombination junction. The open-circuit voltage loss ($\triangle V_{oc,\ loss}$) from tunnel recombination junction additional interfacial recombination as electrical loss ($\triangle V_{oc,\ electrical\ loss}$) and NBG open-circuit voltage optical loss ($\triangle V_{oc,\ NBG\ optical\ loss}$) caused by WBG absorbing visible light (WBG perovskite filtered illuminations)

$\triangle V_{oc,\ loss} = \triangle V_{oc,\ electrical\ loss} + \triangle V_{oc,\ NBG\ optical\ loss} = V_{oc,\ WBG} + V_{oc,\ NBG} - V_{oc,\ tandem}$;

$\triangle V_{oc,\ NBG\ optical\ loss} = V_{oc,\ NBG} - V_{oc,\ NBG\ filter}$;

$\triangle V_{oc,\ electrical\ loss} = V_{oc,\ WBG} + V_{oc,\ NBG\ fiter} - V_{oc,\ tandem} = \triangle V_{oc,\ loss} - \triangle V_{oc,\ NBG\ optical\ loss}$;

NBG subcell $\triangle V_{oc,\ NBG\ optical\ loss}$is 26 mV, which can't be avoided in the tandem devices. $\triangle V_{oc,\ electrical\ loss}$ is 27 mV (**Supplementary Figure 43a** and **Supplementary Table 15**). $\triangle V_{oc,\ electrical\ loss}$ comes from the interface contact loss between two sub-cells with tunnel recombination junction. Passivation of the interface between two sub-cell and tunnel recombination junction will be the way to further reduce the V_{oc} loss.

Optical losses

The optical losses in all-perovskite solar cell is mainly due to the high primary optical

reflection at frond side (1-Reflection (1-R) in **Figure 4d)**, large parasitic absorption losses in front transparent electrode and hole transport layer (PEDOT:PSS) (**Supplementary Figure 43b**), and insufficient light absorption in Pb-Sn perovskite absorber[6]. Optical loss will seriously limit J_{sc} of the tandem device. The J_{sc} values of tandems devices can be further improved by reducing optical reflection via light management (e.g., adding antireflective coating on glass), by using more transparent front electrode and hole transport material (e.g., NiO, PTAA[7] and self-assembled monolayer[8]), and by adopting thicker absorber layer once the carrier diffusion length is sufficiently long.

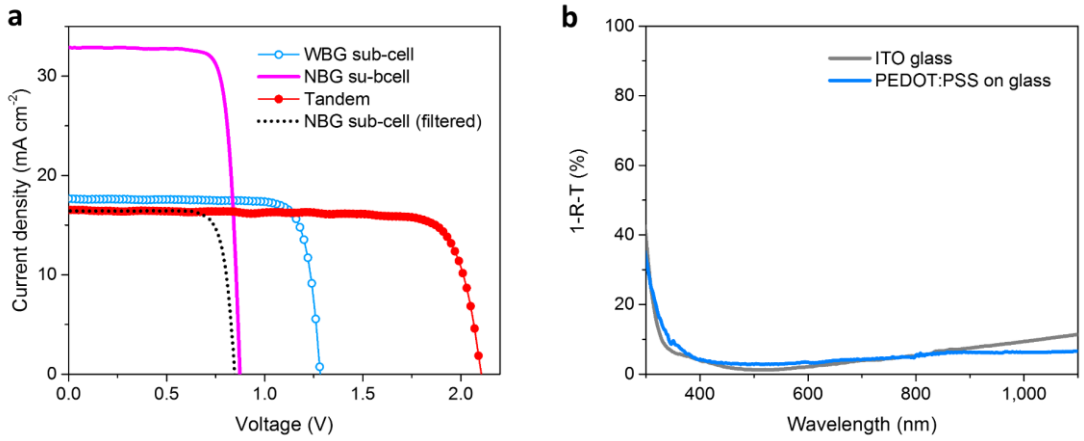

Supplementary Figure 43 | Electrical and optical of tandem device. a, the *J-V* curves of the WBG, NBG, tandem and NBG with WBG filter device (aperture area of 0.049 cm^2 and measured under AM1.5G). **b,** absorption curve of ITO glass and PEDOT:PSS on glass; R is reflection, T is transmission.

Supplementary Figs. 44-45

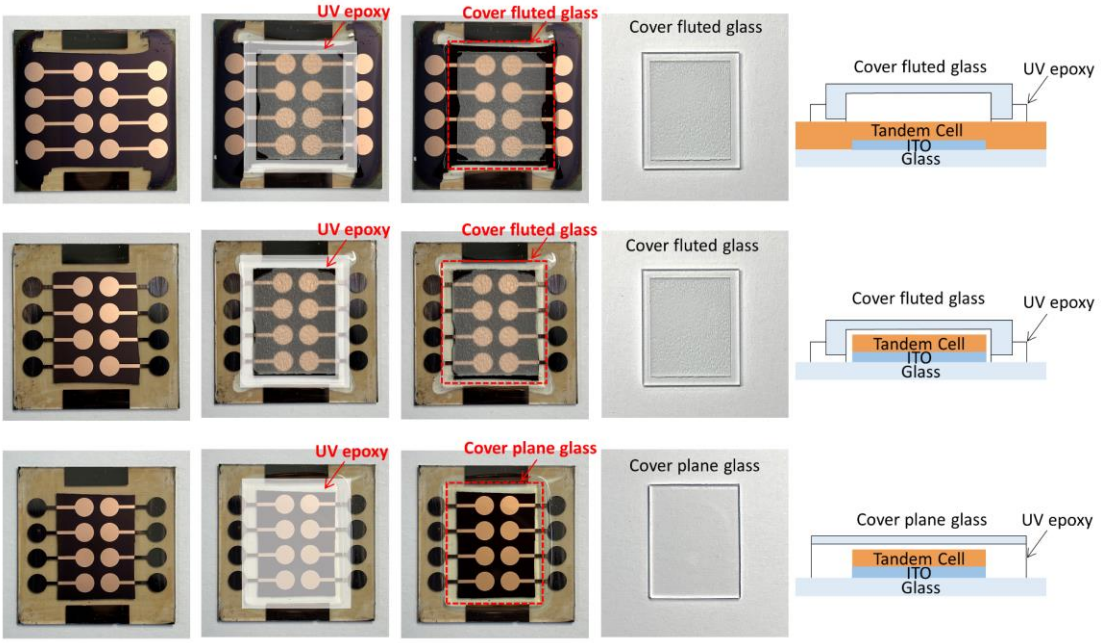

Supplementary Figure 44 | Encapsulation of all-perovskite tandem solar cells. The cover glass has a cavity inside to make sure that there is no direct contact between the active area of solar cell and the cover glass. The UV-epoxy is attached around the edges of cover glass and should not contact with the active area of solar cell. It should be noted that perovskite outside the encapsulation area is better to be removed before the encapsulation. In order to improve the protection effect of the encapsulation, UV-epoxy is applied to the entire active area of solar cell and a plane glass is used for encapsulation. This encapsulation method will cause a slight decrease in device performance.

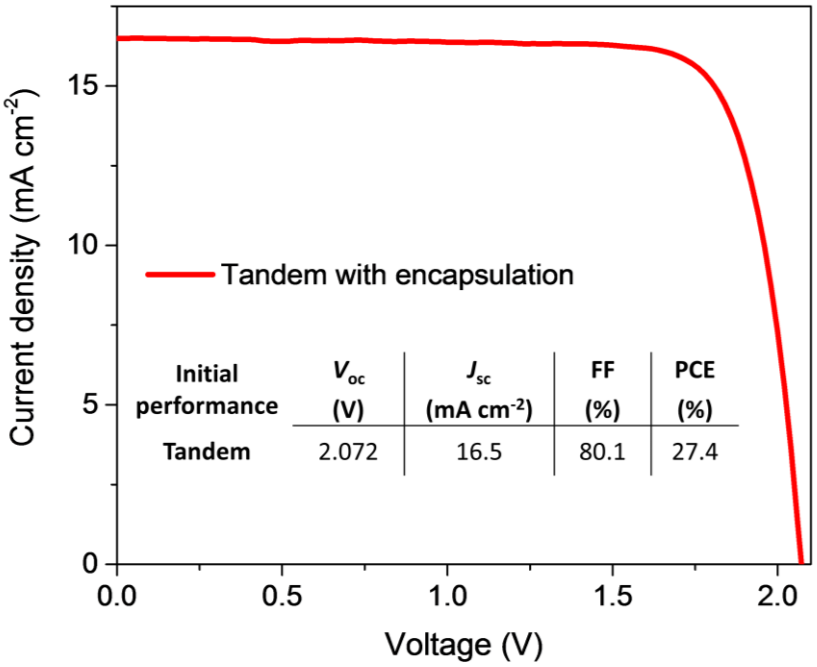

Supplementary Figure 45 | The performance of all-perovskite tandem solar cells with encapsulation before MPP operation.

Supplementary Note 5

PV performance loss from encapsulation

For device encapsulation, UV-epoxy is applied to the entire active area of devices with a plane glass cover (**Supplementary Figure 44**). We observed a slight decrease in FF after encapsulation (**Supplementary Figure 46a**). This loss is likely due to the stress induced on the metal electrode during the UV-epoxy curing process, resulting in poorer contact between the electrode and ETL.

PV performance degradation after MPP tracking

The PCEs of the tandem device decreased after 688 h of operation at MPP (**Supplementary Figure 46b**). Especially, the FF of tandem devices dropped the most after operation. The PV performance degradation could be due to following reasons: (1) In NBG sub-cell, the large amount of MA^+ and the use of PEDOT: PSS as the HTL lead to degradation at elevated temperatures due to sun-light[9–11]; (2) the tunnel recombination junction (ALD-SnO_2/Au/PEDOT: PSS) holds the risk of Au migration into the perovskite absorber layers[11]; (3) in WBG sub-cell, the light-induced halide segregation leads to PV performance degradation.

More technologies to solve PV performance loss and more advanced mechanisms for stability should be developed for all-perovskite tandem in future research.

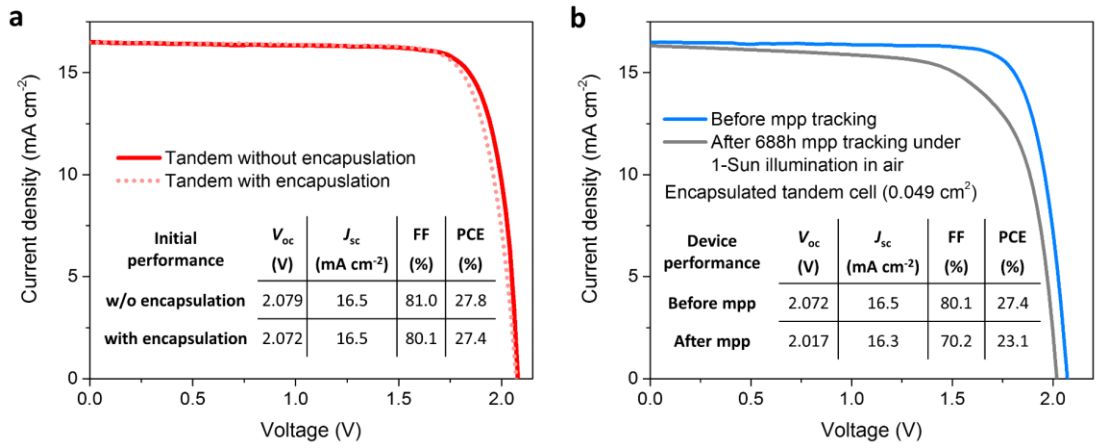

Supplementary Figure 46 | *J-V* curve of tandem device. a, *J-V* curve of tandem device without and with encapsulation. **b,** *J-V* curve of tandem device before and after 688 h MPP tracking operation. The device before mpp tracking is the device with encapsulation (a).

Supplementary Note 6

The reverse bias caused a zener breakdown for all-perovskite tandem solar cells, showing a breakdown voltage of up to ~15V (**Supplementary Figure 47a**). The breakdown voltage of tandems is higher than the sum of the breakdown voltages of two sub-cells (**Supplementary Figure 47c**). We noticed that the reverse breakdown mode of WBG PSCs, NBG PSCs and ~1.55 eV normal bandgap PSCs are thermal breakdown (**Supplementary Figure 47c**), which is irreversible (**Supplementary Figure 47d**). We speculate that the tunnel recombination junction increases reverse breakdown voltage and enhances the reverse bias stability for tandem devices.

The tandem devices showed an obvious degradation immediately after the reverse bias operation (28.3% vs 18.0% in PCEs, origin vs 0 min). However, after 30 minutes storage in the dark, the PCE of the tandem device was recovered back to 27% (**Supplementary Figure 47b** and **Supplementary Table 16**). The recovery of PCE under dark is likely due to the reversibility of ion migration in the perovskite layers[16]. These findings suggest that all-perovskite tandem solar cells have better reverse bias stability than single-junction PSCs.

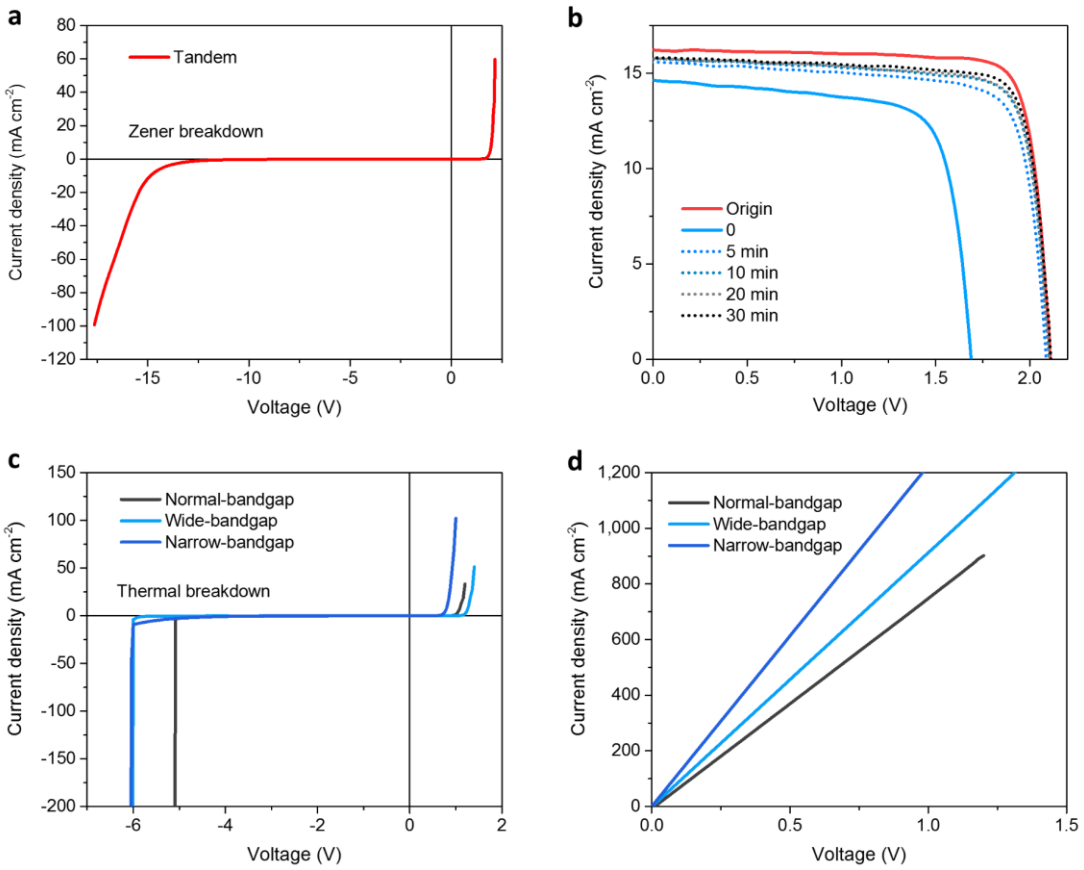

Supplementary Figure 47 | Reverse bias stability of normal-bandgap, sub-cells and tandem devices. a, Dark *J–V* curves showing reverse bias breakdown for tandem device. Reverse bia caused the zener breakdown. **b,** Light *J–V* curves of tandem device when it was fresh, and after reverse bias breakdown 0, 5, 10, 20 and 30 min. **c,** Dark J–V curves showing reverse bias breakdown for wide, narrow sub-cell and normal-bandgap device. Reverse bia caused the irreversible thermal breakdown. **d,** *J–V* curves of single-junction perovskite solar cells after reverse bias breakdown under AM 1.5G illumination.

Supplementary Note 7

Thermal stability under different temperatures

We conducted thermal aging experiments under 85°C and observed an obvious degradation in the PV performance of tandem device (**Supplementary Figure 48a**).We further investigated the operational stability under thermal stress (**Supplementary Figure 48b**), and the device temperature was controlled at 60 or 85 °C by the hot plate. The tandem cells operated at 85°C exhibited a faster degradation compared with operation under 60 °C or room-temperatures under 1-Sun MPP tracking (**Supplementary Figure 48b and Figure 4f**). After 60°C thermal aging and MPP operation, we observed a significant degradation in the photovoltaic performance of tandem devices. The *J-V* curves indicated a similar degradation trend for the tandem devices under both thermal aging at 60°C and MPP operation at 60°C (**Supplementary Figure 48c, d**). The collective decline of V_{oc}, $J_{sc,}$ and FF contributed to the performance degradation of tandem devices. However, the photovoltaic performance of tandem device degraded more significantly under 60°C MPP operation than the 60°C thermal aging process. This suggests that illumination had further contributed to the degradation of the performance, which requires further investigation in the future.

The effect of Br diffusion

Previous studies indicate that the introduction of Br into metal iodide perovskites will change the energy-band position of perovskite[12]. We observed that the small amount of Br diffusion from FL-WBG perovskite into the bottom Pb-Sn perovskite layer occurred during the initial stages of device preparation, but it tended to be homogenized within the perovskite layers and did not degrade the device performance (**Supplementary Figure 18-20**).

Analysis of the degradation

We carried out XPS measurements of PHJ perovskite films to verify whether Sn^{2+} could diffuse through the FL-WBG perovskite layer. In the case of light soaking with WBG filter or heating at 85 ºC, we didn't observe any signal of Sn^{2+} on FL-WBG perovskite after stressing for 264 h (**Supplementary Figure 49a, b**). Furthermore, we did not observe any signal of Sn^{2+} on FL-WBG after 60 days of dark storage (**Supplementary Figs. 15-16**). The suppressed Sn ion migration can be attributed to the high activation energy required for the migration of B-site ions[13,14]. Additionally, electrical bias is also unlikely to induce obvious diffusion of Sn ions into the FL-WBG perovskite in devices, as we did not observe faster degradation in PHJ devices compared to control devices (**Supplementary Figure 48b**). Our previous work showed that device thermal instability is attributed to the back- electrodes metal ion and tunnel recombination

junction metal ion diffusion[11], thermal instability of MA and PEDOT:PSS from Pb-Sn device[11,15].

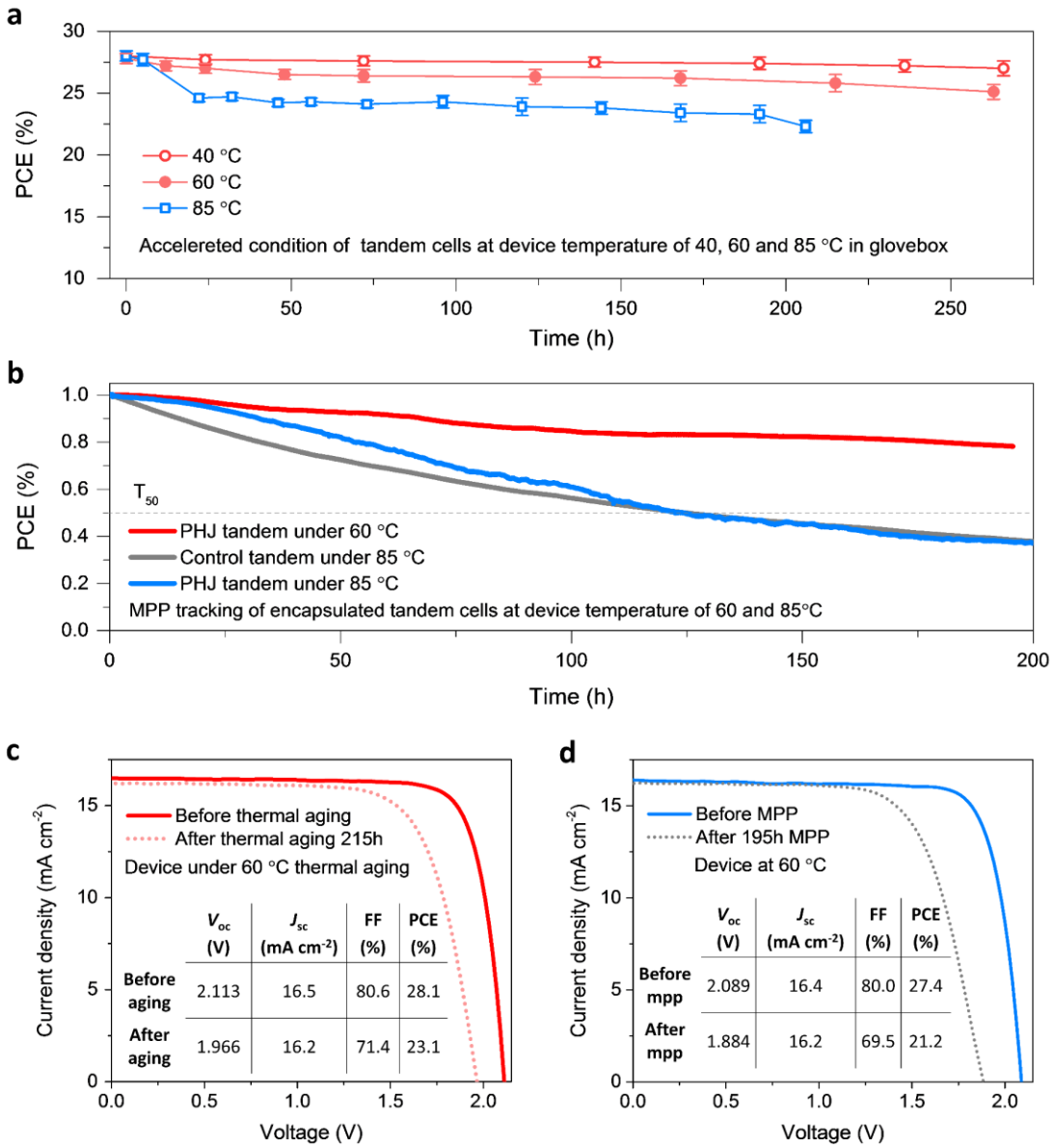

Supplementary Figure 48 | Stability of tandem device under accelerated conditions. **a,** Performance evolution of all-perovskite tandem solar cells aging at 40, 60 and 85 °C on a hot plate and under dark in the N_2 glovebox. **b,** Continuous maximum power point (MPP) tracking of encapsulated tandem solar cells at device temperatures of 60 and 85°C for ~200 hours under simulated AM1.5G illumination (100 mW cm^{-2}, multi-color LED simulator) in ambient air with a humidity of 20-40%. **c,** *J-V* curve of tandem device before and after 215h thermal aging under 60 °C. **d,** *J-V* curve of tandem device before and after 195 h MPP tracking operation under 60 °C.

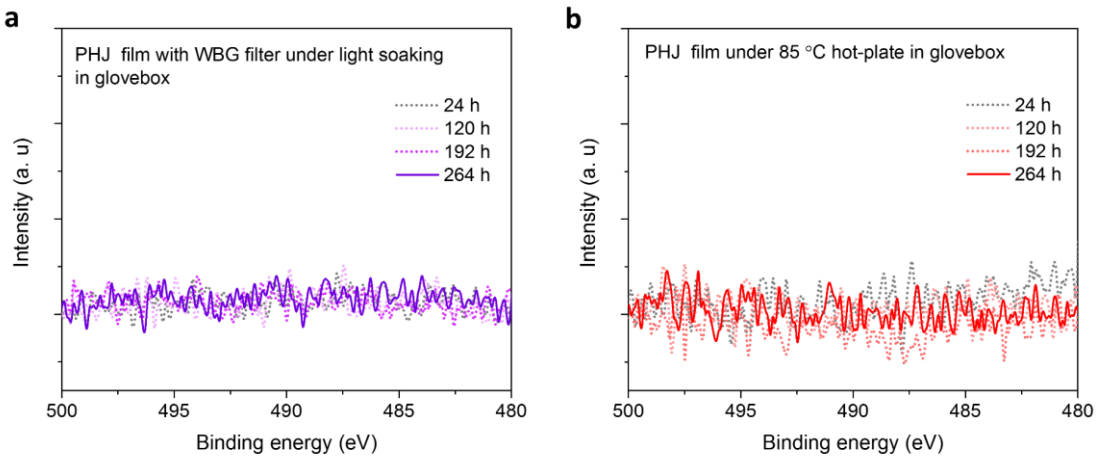

Supplementary Figure 49 | XPS of PHJ films after light soaking and thermal aging. Sn $3d_{5/2}$ XPS spectra of PHJ perovskite films under light soaking with WBG filter (a), and under 85°C heating (b) for 24, 120, 192, and 264 hours.

Supplementary Tables 1-16

Supplementary Table 1 Performance of control and HPJ device. The FL-WBG perovskite films with various content of FABr/FAI ions in the organic salt.

FABr/FAI	V_{oc} (V)	J_{sc} (mA cm^{-2})	FF (%)	PCE (%)
Control	0.831	79.7	32.1	21.3
2.5:1	0.697	70.6	27.6	13.6
2:1	0.805	76.4	30.9	19.0
1.5:1	0.812	79.6	31.0	20.1
1:1	0.878	80.7	32.8	23.2

Supplementary Table 2 Performance of PHJ Pb-Sn perovskite solar cells with various thickness PbI_2/CsBr inorganic layer. 15 devices for each type (show in **Supplementary Figure 8).**

PbI_2/CsBr inorganic thickness (nm)	FL-WBG thickness (nm)	V_{oc} (V)	J_{sc} (mA cm^{-2})	FF (%)	PCE (%)
Control	/	0.832±0.07	32.4±0.4	79.1±0.6	21.4±0.3
10	/	0.841±0.09	32.3±0.5	79.2±0.9	21.5±0.6
30	50	0.863±0.06	32.4±0.4	81.0±0.6	22.6±0.2
50	80	0.828±0.06	32.2±0.2	79.4±0.6	21.2±0.3
100	160	0.827±0.06	30.9±0.2	77.8±0.6	19.8±0.3

Supplementary Table 3 Performance of PHJ and control Pb-Sn PSCs without and with PEAI post-treatment (shown in Supplementary Figure 12 and Supplementary Figure 13).

Device	V_{oc} (V)	J_{sc} (mA cm^{-2})	FF (%)	PCE (%)
PHJ without PEAI	0.862±0.05	32.5±0.3	80.2±0.7	22.5±0.2
PHJ with PEAI	0.861±0.04	32.5±0.3	81.2±0.03	22.7±0.3
Control without PEAI	0.838±0.01	32.3±0.4	80.1±0.6	21.7±0.5
Control with PEAI	0.837±0.01	31.5±0.8	77.5±0.6	20.5±0.7

Supplementary Table 4 Photovoltaic performance of control and PHJ mixed Pb-Sn perovskite solar cells (shown in Fig. 1e). Average performance of 26 devices.

Device	V_{oc} (V)	J_{sc} (mA cm^{-2})	FF (%)	PCE (%)
Control Average	0.824±0.006	32.5±0.3	78.5±0.7	21.0±0.3
PHJ Average	0.869±0.004	32.4±0.4	80.8±0.8	22.8±0.4

Supplementary Table 5 Photovoltaic performance of control and PHJ with different ETL. Control_BCP, Control_ALD-SnO_2, PHJ_BCP and PHJ_ALD-SnO_2 mixed Pb-Sn perovskite solar cells with an absorber thickness of ~1,200 nm. Typical *J-V* Curve for each type is presented as well (shown in **Supplementary Fig. 18**).

Device	V_{oc} (V)	J_{sc} (mA cm^{-2})	FF (%)	PCE (%)
Control_BCP	0.839	79.6	32.5	21.7
Control_ALD-SnO_2	0.820	78.5	32.5	20.9
PHJ_BCP	0.873	81.1	32.6	23.1
PHJ_ ALD-SnO_2	0.880	81.1	32.5	23.2

Supplementary Table 6 Material parameters used for simulation in SCAPS-1D[17,18].

Parameter	PEDOT:PSS	NBG	FL-WBG	C_{60}
Thickness (nm)	30 nm	1,200 nm	30 nm	25 nm
Bandgap (eV)	1.8	1.25	1.62	1.7
Electron Affinity (eV)	3.46	4.03	4.17	3.9
Dielectric permittivity (relative)	18.7	10	30	4.2
Conduction band effective density of states (cm^{-3})	2.2E18	1.2E19	2.75E18	8E19
Valence band effective density of states (cm^{-3})	1.8E19	2.9E18	3.8E18	8E19
Electron mobility ($cm^2V^{-1}s^{-1}$)	1.8E-3	11.7	10	8.0E-2
Hole mobility ($cm^2V^{-1}s^{-1}$)	1.8E-2	70.3	10	3.5E-3
Shallow uniform acceptor density, *N*A (cm^{-3})	1.0E18	1E17	10E9	0
Shallow uniform donor density, *N*D (cm^{-3})	0	1E13 (0)	10E9	2.6E17
Defect type	Neutral	Neutral	Neutral	Neutral
Capture cross section (electrons) (cm^{-3})	1E14	1E14	1E14	1E14
Capture cross section (hole) (cm^{-3})	1E14	1E14	1E14	1E14
Energetic distribution	Single	single	Single	single
Energy level (eV)	0.6	0.6	0.6	0.6
Total defect density (cm^{-3})	1E16	2.5E15	1E14	1E14

Supplementary Table 7 Simulated *J-V* curves of the control mixed Pb–Sn perovskite solar cells with DIL for different defect densities. The parameters of the simulation were set to be identical with **Supplementary Fig 28**.

Control N_{def} (cm^{-3})	V_{oc} (V)	J_{sc} (mA cm^{-2})	FF (%)	PCE (%)
1×10^{14}	0.872	33.5	85.1	24.9
5×10^{14}	0.871	33.5	84.9	24.8
1×10^{15}	0.871	33.5	84.8	24.8
5×10^{15}	0.868	33.5	83.7	24.4
1×10^{16}	0.864	33.5	82.7	23.9
5×10^{16}	0.836	33.5	78.9	22.1
1×10^{17}	0.811	33.5	77.7	21.1
5×10^{17}	0.736	33.5	75.3	18.6
1×10^{18}	0.701	33.5	74.1	17.4

Supplementary Table 8 Simulated *J-V* curves of the PHJ mixed Pb–Sn perovskite solar cells with DIL for different defect densities. The parameters of the simulation were set to be identical with **Supplementary Fig 28**.

PHJ N_{def} (cm^{-3})	V_{oc} (V)	J_{sc} (mA cm^{-2})	FF (%)	PCE (%)
1×10^{14}	0.877	33.5	85.5	25.1
5×10^{14}	0.877	33.5	85.4	25.1
1×10^{15}	0.877	33.5	85.4	25.1
5×10^{15}	0.877	33.5	85.4	25.1
1×10^{16}	0.877	33.5	85.3	25.1
5×10^{16}	0.876	33.5	84.7	24.9
1×10^{17}	0.875	33.5	84.0	24.6
5×10^{17}	0.867	33.5	79.5	23.1
1×10^{18}	0.857	33.5	75.6	21.7

Supplementary Table 9 Simulated *J-V* curves of the control mixed Pb–Sn perovskite solar cells with different thickness DIL. The parameters of the simulation were set to be identical with **Supplementary Fig 29**.

Control DIL thickness (nm)	V_{oc} (V)	J_{sc} (mA cm^{-2})	FF (%)	PCE (%)
w/o IDL	0.872	33.5	85.1	24.9
0.2	0.857	33.5	81.3	23.4
0.5	0.837	33.5	79.0	22.2
1	0.811	33.5	77.7	21.1
1.5	0.793	33.5	76.9	20.4
2	0.779	33.5	76.3	19.9
2.5	0.767	33.5	75.8	19.5
3	0.758	33.5	75.4	19.2
4	0.745	33.5	74.6	18.6

Supplementary Table 10 Simulated *J-V* curves of the PHJ mixed Pb–Sn perovskite solar cells with different thickness DIL. The parameters of the simulation were set to be identical with **Supplementary Fig 29**.

PHJ DIL thickness (nm)	V_{oc} (V)	J_{sc} (mA cm^{-2})	FF (%)	PCE (%)
w/o DIL	0.877	33.5	85.4	25.1
0.2	0.877	33.5	85.1	25.0
0.5	0.876	33.5	84.7	24.9
1	0.875	33.5	84.0	24.6
1.5	0.874	33.5	83.3	24.4
2	0.872	33.5	82.9	24.2
2.5	0.870	33.5	82.5	24.0
3	0.869	33.5	82.0	23.9
4	0.865	33.5	81.3	23.5

Supplementary Table 11 Summary of measured and calculated solar cells EQE_{EL} parameters. Based on the detailed balance theory, the voltage loss in solar cells can be attributed to the three factors[19–21].

	Control	PHJ
E_g (eV)	1.25	1.25
ΔV_1 (mV) $(E_{gap} - qV_{OC}^{SQ})$	256	256
ΔV_2 (mV) $(q \triangle V_{OC}^{rad,below\ gap})$	27	27
ΔV_3 (mV) $(q \triangle V_{OC}^{non-rad})$	147	97
V_{oc} (V)	0.821	0.873
$V_{oc}+\Delta V_1+\Delta V_2+\Delta V_3$ (V)	1.251	1.253

Supplementary Table 12 Simulation photovoltaic performance of tandem perovskite solar cells with different subcells. The *J-V* curves of device shown in **Supplementary Fig. 36c**.

Device	V_{oc} (V)	J_{sc} (mA cm^{-2})	FF (%)	PCE (%)
WBG 1 / NBG 1	2.119	16.5	**76.6**	26.8
WBG 2 / NBG 1	2.130	16.5	**78.5**	27.6
WBG 1 / NBG 2	2.119	16.5	**79.9**	28.0
WBG 2 / NBG 2	2.131	16.4	**83.1**	29.3

Supplementary Table 13 Photovoltaic performance of tandem perovskite solar cells with different subcells. The *J-V* curves of device shown in **Supplementary Fig. 38c**.

Device	V_{oc} (V)	J_{sc} (mA cm^{-2})	FF (%)	PCE (%)
NiO-VNPB WBG / Control NBG	2.035	16.4	78.0	26.0
NiO-SAM WBG / Control NBG	2.073	16.5	78.9	27.0
NiO-VNPB WBG / PHJ NBG	2.064	16.5	81.4	27.7
NiO-SAM WBG / PHJ NBG	2.100	16.4	82.5	28.4

Supplementary Table 14 Photovoltaic performance of control and PHJ tandem perovskite solar cells with an absorber thickness of ~1,200 nm. Average performance of 26 devices and Typical *J-V* Curve for each type is presented as well (shown in **Fig. 4b**).

Device	V_{oc} (V)	J_{sc} (mA cm^{-2})	FF (%)	PCE (%)
Control tandem Average	2.049±0.01	16.3±0.1	79.3±0.5	26.5±0.3
PHJ tandem Average	2.099±0.01	16.3±0.1	81.7±0.6	27.9±0.3

Supplementary Table 15 Photovoltaic performance of WBG, NBG, tandem and NBG with filter device.

Device performance	V_{oc} (V)	J_{sc} (mA cm^{-2})	FF (%)	PCE (%)
WBG sub-cell	1.284	17.7	81.4	18.5
NBG sub-cell	0.872	32.9	81.6	23.4
Tandem	2.103	16.5	81.3	28.2
NBG sub-cell with filter	0.846	16.4	81.2	11.3
$\triangle V_{oc,\ loss}$ (V)		0.053		
$\triangle V_{oc,\ NBG\ optical\ loss}$ (V)		0.026		
$\triangle V_{oc,\ electrical\ loss}$ (V)		0.027		

Supplementary Table 16 The PV performance of all-perovskite tandem device after reverse bias operation.

	V_{oc} (V)	J_{sc} (mA cm^{-2})	FF (%)	PCE (%)
Origin	2.108	16.2	82.7	28.3
0	1.688	14.6	73.1	18.0
5 min	2.083	15.6	76.9	25.0
10 min	2.101	15.8	79.1	26.2
20 min	2.102	15.8	79.6	26.4
30 min	2.111	15.8	80.8	27.0

References

1. Xiao, K. *et al.* All-perovskite tandem solar cells with 24.2% certified efficiency and area over 1 cm^2 using surface-anchoring zwitterionic antioxidant. *Nat. Energy* **5**, 870–880 (2020).
2. Santbergen, R. *et al.* GenPro4 optical model for solar cell simulation and its application to multijunction solar cells. *IEEE J. Photovoltaics* **7**, 919–926 (2017).
3. Gao, Y. *et al.* Performance optimization of monolithic all-perovskite tandem solar cells under standard and real-world solar spectra. *Joule* **6**, 1944–1963 (2022).
4. Rühle, S. Tabulated values of the Shockley-Queisser limit for single junction solar cells. *Sol. Energy* **130**, 139–147 (2016).
5. Stolterfoht, M. *et al.* Approaching the fill factor Shockley-Queisser limit in stable, dopant-free triple cation perovskite solar cells. *Energy Environ. Sci.***10,** 1530–1539 (2017).
6. Yang, Z. *et al.* Enhancing electron diffusion length in narrow-bandgap perovskites for efficient monolithic perovskite tandem solar cells. *Nat. Commun.* **10**, 4498 (2019).
7. Werner, J. *et al.* Improving low-bandgap tin-lead perovskite solar cells via contact engineering and gas quench processing. *ACS Energy Lett.* **5**, 1215–1223 (2020).
8. Al-Ashouri, A. *et al.* Conformal monolayer contacts with lossless interfaces for perovskite single junction and monolithic tandem solar cells. *Energy Environ. Sci.* **12**, 3356–3369 (2019).
9. Liu, X. *et al.* Improved efficiency and stability of Pb-Sn binary perovskite solar cells by Cs substitution. *J. Mater. Chem. A* **4**, 17939–17945 (2016).
10. Prasanna, R. *et al.* Design of low bandgap tin–lead halide perovskite solar cells to achieve thermal, atmospheric and operational stability. *Nat. Energy* **4**, 939–947 (2019).
11. Gao, H. *et al.* Thermally stable all-perovskite tandem solar cells fully using metal oxide charge transport layers and tunnel junction. *Sol. RRL* **5**, 1–8 (2021).
12. Lee, S. *et al.* Inorganic narrow bandgap $CsPb_{0.4}Sn_{0.6}I_{2.4}Br_{0.6}$ perovskite solar cells with exceptional efficiency. *Nano Energy* **77**, 105309 (2020).
13. Eames, C. *et al.* Ionic transport in hybrid lead iodide perovskite solar cells. *Nat. Commun.* **6**, 2–9 (2015).
14. Ighodalo, K. O. *et al.* Negligible ion migration in tin-based and tin-doped perovskites. *Angew. Chemie. Int. Ed.* **62**, e202213932 (2023).
15. Wu, P. *et al.* Efficient and thermally stable all-perovskite tandem solar cells using all-FA narrow-bandgap perovskite and metal-oxide-based tunnel junction. *Adv. Energy Mater.* **12**, 220948 (2022).
16. Razera, R. A. Z. *et al.* Instability of p-i-n perovskite solar cells under reverse bias. *J. Mater. Chem. A* **8**, 242–250 (2020).
17. Zhang, W. *et al.* Revealing key factors of efficient narrow-bandgap mixed lead-tin perovskite solar cells via numerical simulations and experiments. *Nano Energy* **96**, 107078 (2022).

18. Deepthi Jayan, K. & Sebastian, V. Comprehensive device modelling and performance analysis of MASnI3 based perovskite solar cells with diverse ETM, HTM and back metal contacts. *Sol. Energy* **217**, 40–48 (2021).
19. Zhang, X. *et al.* The Voltage Loss in Tin Halide Perovskite Solar Cells: Origins and Perspectives. *Adv. Funct. Mater.* **32**, (2022).
20. Liu, J. *et al.* Fast charge separation in a non-fullerene organic solar cell with a small driving force. *Nat. Energy* **1**, 16089 (2016).
21. Mahesh, S. *et al.* Revealing the origin of voltage loss in mixed-halide perovskite solar cells. *Energy Environ. Sci.* **13**, 258–267 (2020).